Coalescence in fused filament fabrication process: thermo-dependent characterization of high-performance polymer properties

Arthur Lepoivre, Arthur Lévy, Nicolas Boyard, Vincent Gaudefroy, Vincent Sobotka

Coalescence in fused filament fabrication process: thermo-dependent characterization of high-performance polymer properties

Arthur Lepoivre[1,2], Arthur Levy[1*], Nicolas Boyard[1], Vincent Gaudefroy[3], Vincent Sobotka[1]

[1] *Université de Nantes, CNRS, Laboratoire de thermique et énergie de Nantes, LTeN, UMR 6607, F-44000 Nantes, France*

[2] *Institut de Recherche Technologique Jules Verne, 44340 Bouguenais, France*

[3] *Université Gustave Eiffel, Département MAST, Allée des Ponts et Chaussées, 44344 Bouguenais, France*

* Corresponding author: arthur.levy@univ-nantes.fr

Abstract

One of the major drawbacks of the thermoplastic Fused Filament Fabrication process (FFF) is the poor mechanical properties of the parts produced. This is mostly related to the macroporosities resulting from a limited coalescence between filaments. Coalescence is ruled by the viscosity and surface tension of a polymer. Thus, an accurate characterization of these two properties is required to model and optimize coalescence during filament deposition and cooling. In this work, a surface tension characterization procedure over a large temperature range (25–380 °C) is presented and applied to PolyEtherKetoneKetone (PEKK) material. Additionally, the Newtonian viscosity is characterized with rheometry. The coalescence is then simulated by coupling an existing semi-analytical model with a previously presented 2D heat transfer finite element simulation model.
The results show the importance of the temperature dependent implementation of surface tension. Additionally, a parametric study provides an industrial understanding of the FFF process.

Keywords: Additive Manufacturing; Fused Filament Fabrication; Coalescence; Surface Tension; Characterization

1. Introduction

Fused Filament Fabrication (FFF) is an additive manufacturing process. Including other processes, such as stereolithography and selective laser melting, all additive manufacturing products and services will reach $15.8 billion USD in revenue in 2020 and $35.6 billion USD in 2024 [1]. FFF has applications in the health, automotive, aeronautical, and prototyping industries. This process was invented in 1992 [2] and involves the manufacturing of 3D polymer parts by extruding a melted thermoplastic filament through a nozzle. The toolpath of the nozzle is specifically designed to create particular parts. The filament is heated by an extrusion unit that brings the polymer to either a viscous or molten state, for the manufacturing of amorphous and semi-crystalline polymers, respectively. After deposition, the filament solidifies as it cools

down with its environment and additional layers can be subsequently deposited. This process offers the advantage of producing parts with complex geometry, with a wide choice of materials, and without requiring the use of a molding cavity. However, this process has several drawbacks. First, the sizes of the manufactured parts are limited and the manufacturing cycles are long. Currently, the most limiting aspect is the poor mechanical properties obtained, especially when compared to other manufacturing processes, such as injection molding.

Many authors have worked on the influence of slicing parameters and path generation on the final mechanical properties [3,4]. However, even with an optimized path, the final mechanical properties are mostly governed by the adhesion quality at the filament scale.

Sun *et al*. [5] described the adhesion in the FFF process as the succession of several steps: intimate contact, coalescence, and healing with a random distribution of the molecular polymer chains on either side of the interface (Figure 1).

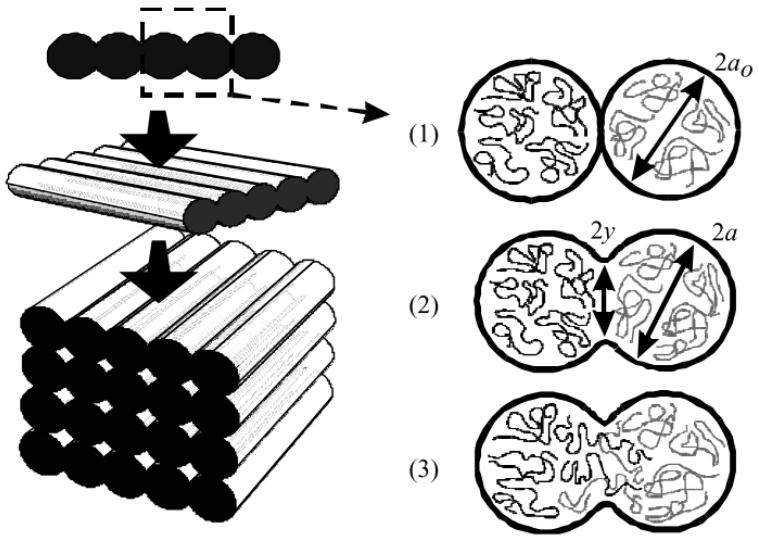

Figure 1 – Adhesion mechanism between two filaments in the FFF additive manufacturing process. (1) Contact between the two filaments, (2) coalescence, and (3) healing with molecular interdiffusion at the interface [5].

The coalescence mechanism, illustrated by step 2 in Figure 1, is a prerequisite for the subsequent healing stage for proper adhesion. The coalescence of two filaments can be quantified by the contact angle between the two filaments.

The first model was developed by Frenkel and Eshelby in 1949 [6,7], it described an ideal coalescence for a Newtonian viscous incompressible fluid between two spheres. The model considers a uniform strain tensor in the system. Under an isothermal assumption, physical properties are constant. To solve this analytical model, an approximation is done for small angles θ. Later, Pokluda *et al.* [8] solved the equation for finite angles using a Runge-Kutta-

Fehlberg numerical method. Alternatively, Hopper [9] described the coalescence of two cylinders using an ellipse parametric equation. His second model [10,11] describes the coalescence between two infinite cylinders assuming a Newtonian Stokes flow, without inertia, and with surface tension forces as the only driving force.

All of these coalescence models assume that a viscous polymer is subject to surface tension. Thus, it is of primary importance to accurately characterize these two material properties up to processing temperatures.

Aeronautical grade thermoplastics, such as the PolyArylEtherKetone (PAEK) family, are commonly used to manufacture structural or semi-structural parts. Their processing with FFF is challenging for two reasons: 1) they require high processing temperatures [12,13]; 2) a good final mechanical quality is required to fulfill aeronautical requirements.

During coalescence, the surface tension has the opposite effect of viscous forces. Bakrani Balani [14] numerically showed the importance of surface tension for PolyEtherEtherKetone (PEEK) 450G, as it varied from $\gamma = 10$ to $25\ mN/m$, on the coalescence process. Thus, to accurately model the coalescence process, surface tension and viscosity must be characterized along with their temperature dependencies.

In this study, the characterization was performed by a shape-analyzing method for a hanging or deposited liquid drop or bubble over a large range of temperatures.

The surface tensions of PAEK polymers at room and at processing temperatures have been characterized several times in existing works, as summarized in Table 1.

Authors and year	**Material**	**Characterization temperature**	**Surface tension, (mN/m)**	**Characterization details**
Sauer, Dipaolo (1991) [15]	PEKK (DuPont) $\overline{M_n}$ = 9 kg/mol)	25 °C	45.3 ± 1 with γ_D=41.7	2 reference liquids
Bowditch (1996) [16]	PEEK film	Room temperature assumed	38.7 ± 6.1 with γ_D=31.5	4 reference liquids
Ha *et al*. (1997) [17]	Semi-crystalline PEEK film (Litrex)	Room temperature assumed	33.6 with γ_D=18.7	Goniometer ERMA Optical with 2 reference liquids (6 measurements)
Iqbal *et al*. (2010) [18] and Bhatnagar *et al*. (2011) [19]	PEEK sheet	Room temperature assumed	51.1 with γ_D=46.8	CAM 200 Optical Tensiometer with 2 reference liquids
Kluska *et al*. (2014) [20]	Borapeek PEEK	Room temperature assumed	43.7 ± 0.8 with γ_D=41.2	DSA 10 MK2 (KRÜSS) with 2 reference liquids (7 measurements per liquid)
Su *et al*. (2017) [21]	Victrex PEEK film	Room temperature assumed	37 ± 3 with γ_D=34	DataPhysics OCA 20 contact angle system, 5 specimens with 3 reference liquids
	Cytec PEKK film		39 ± 4 with γ_D=35	
Bakrani Balani (2019) [14]	Victrex PEEK film	Room temperature	38.7 ± 3 with γ_D=35.1	GBX DigiDrop surface tensiometer
Sauer, Dee (2002) [22]	PEKK (DuPont)	298 - 345 °C	(-0.08×T+63.8) 36.2 at 345 °C	2 reference liquids
Sauer, Dipaolo (1991) [15]	PEKK (DuPont)	350 °C	24.2 ± 1.5 (4 measure-ments)	Wilhelmy method with a homemade bench, temperature regulated with a hot plate at 390 °C, temperature checked with a small thermocouple near the polymer surface (average of 30 s intervals with 10 pts/s)
Defauchy (2013) [23]	Low viscosity PEEK 150 Xf (Victrex)	367 °C	32.2 ± 2.5 (10 measure-ments)	Pendant drop method with Digidrop GBX, temperature regulation of the metallic syringe and the heating chamber

Table 1 – Surface tension measurements at room temperature and high temperature, as reported in the literature for the PAEK family of polymers.

The results in Table 1 at ambient temperature were obtained with the contact angle method. An average surface tension of $\gamma_{room\ temperature} = 40.9\ mN/m$ with a 52% variation between the minimum and maximum values can be inferred from these literature values.

Measuring the surface tension of molten polymers at the PAEK processing temperature (over 300 °C) is challenging. On the one hand, it exceeds the temperature range permitted by standard apparatuses, while on the other hand, the viscosities of these polymers are high. Moreover, measurements at high temperatures must be carried out quickly to avoid surface degradation, oxidation, or crosslinking [15]. Only three PAEK polymer surface tension values at high temperatures were found in the literature [15,22,23], as shown in Table 1. They have a 59% variation for the temperature range of 345–367 °C; this could be due to different polymer molecular masses, which were not mentioned by the authors.

Surface tension linearly decreases with temperature and can be modeled using different theories based on studies by Eötvös [24], Guggenheim [25], or Macleod [26]. Compared to pure liquids that were reference materials in the literature, polymers have long polymer chains and high molecular masses. Surface tension increases as the molecular mass increases, as was first modeled by Legrand and Gaines [27] and experimentally observed by several authors [22,28,29]. Surface tension can also be predicted theoretically with the Parachor method, where the unit Parachor for each atom or double bond are given in abacuses. Quayle [30] compared the principal values used by Sugden [31], Mumford & Phillips [32], and Vogel [33] and determined the most adequate values for use. In addition to its lack of a theoretical basis, the Parachor methodology is also controversial because it does not consider the molecular mass influence. However, the method is advantageous in terms of its accuracy, even with only a few parameters. The Parachor values found in the literature for PAEK polymers are presented in Table 2.

Authors and year	Material	Parachor value $(cm^3/mol)\cdot(erg/cm^2)^{1/4}$	Characterization temperature	Surface tension value (mN/m)	Method details
Bakrani Balani (2019) [14]	PEEK 450G (Victrex)	551.2	360 °C	18 ± 3	**Method:** Parachor **Input parameters:** Parachor, P, constant density, ρ, and molar mass, M
Cazaux (2017) [34]	PEKK ($\overline{M_n}$=50 kg/mol)	616.4	320 °C	35.0	**Method:** Le Grand & Gaines **Input parameters:** Parachor, P, temperature, T, average molecular mass, $\overline{M_n}$, and surface tension for infinite molecular mass, γ_∞

Table 2 – Surface tension determination with theoretical approaches, as reported in the literature.

The molecular weight and temperature dependence of surface tension might explain the high variability (more than 50%) of the surface tension reported in the literature. This shows the necessity to perform a fine characterization on the material that will be used, instead of just using the values presented in the literature for other materials.

The other important property required to characterize coalescence is the viscosity of the polymer. Viscosity is usually determined by measuring the viscoelastic behavior of the polymer with a rotational rheometer [35]. Polymers viscosity strongly depends on the molecular weight of the polymeric chain [36] and thus can vary for a same repetitive unit. ARKEMA® commercialized several PEKK grades with different viscosities values [37]. Some determinations of the Newtonian viscosity were found in the literature for grade PEKK KEPSTAN® 6002 [38], and also for PEKK KEPSTAN® 6003 and 7003 [39], but no values were found for the PEKK KEPSTAN® 6004 grade considered in this study. Although this requires great care in the characterization, and specifically concerning the aging of the polymer, the methodology remains standard and does not present any other challenges concerning PAEK specificity.

The first section of this paper describes the characterization of surface tension and viscosity of an aeronautical grade PEKK polymer up to its processing temperature. The second section details a dimensional analysis of the coalescence time followed by a parametric study that

makes use of the characterized properties and shows the temperature influence. The parametric study yields technological results that are applicable to the adhesion of two filaments in the FFF process.

2. Characterization of coalescence properties

This work focused on PEKK KEPSTAN® 6004 material supplied by ARKEMA with a terephthalate (T) to isophthalate (I) chemical group ratio of 60/40. Due to its high viscosity, the coalescence flow can be modeled with an incompressible Stokes flow. Under this assumption, viscosity and surface tension must be characterized up to 380 °C, the maximum processing temperature recommended by the supplier.

2.1. Surface tension measurement

The surface tension was determined experimentally with two approaches: the sessile drop method for low temperatures (at 25 and 80 °C) and the pendant drop method for higher ones (from 320 to 370 °C). Both methodologies are standard. For the sessile drop, several reference liquids, with known surface tension values, are used to determine the surface tension of the material to characterize. For the pendant drop, the novelty is to use this methodology at high temperature, and with a thermal instrumentation that was added to the measuring apparatus.

2.1.1. Sessile drop method for low temperatures

A droplet of reference liquid was deposited onto a flat solid substrate to be characterized. The surface tension was determined from the contact angle, θ, measured between the droplet and the substrate (Figure 2).

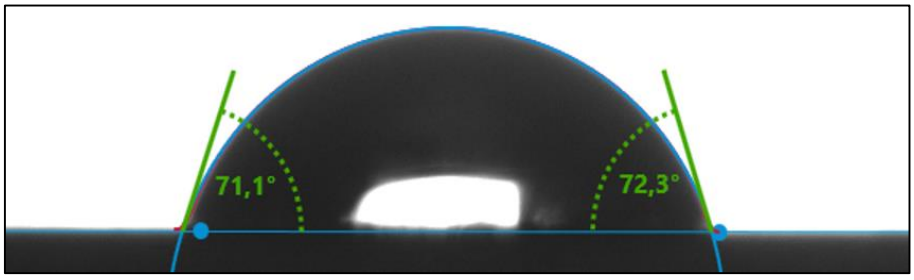

Figure 2 – Contact angle measurement of a water drop on a PEKK substrate, at 25 °C.

Usually, only the reference liquid surface tension, γ_L, is known and both the liquid-solid interfacial energy, γ_{LS}, and the surface tension of the solid, γ_S, are unknown. First, the energy of adhesion, W_a, defined by the Dupré equation:

$$W_a = \gamma_L + \gamma_S - \gamma_{LS} \quad (1)$$

and Young-Dupré equation:

$$W_a = \gamma_L \times (1 + cos\,\theta) \quad (2)$$

was used.

Then, according to Owens, Wendt, Rabel and Kaelble (OWRK) theory [40], the surface tension was described as the sum of the polar and dispersive components, γ^P and γ^D, respectively:

$$\gamma = \gamma^P + \gamma^D \quad (3)$$

The polar component is due to dipole-dipole interactions, hydrogen bonds, and Lewis acid-base interactions, as opposed to the dispersive component, which is caused by weak van der Waals interactions (including Keesom, Debye, and London forces). The OWRK theory was also used to define the adhesion energy as a geometric mean of the polar and dispersive components:

$$W_a = 2\left(\sqrt{\gamma_S^D \times \gamma_L^D} + \sqrt{\gamma_S^P \times \gamma_L^P}\right) \quad (4)$$

From Equations (2) and (4), the fundamental equation of the OWRK theory can be written:

$$\underbrace{\frac{\gamma_L(1 + cos\theta)}{2\sqrt{\gamma_L^D}}}_{y_{OWRK}} = \sqrt{\gamma_S^P} \times \underbrace{\frac{\sqrt{\gamma_L^P}}{\sqrt{\gamma_L^D}}}_{x_{OWRK}} + \sqrt{\gamma_S^D} \quad (5)$$

With the experimental contact angles, θ, the left-hand side of Equation (5) was plotted for several reference liquids with a known ratio of $\sqrt{\gamma_L^P}$ / $\sqrt{\gamma_L^D}$. A linear regression then provided the polar, γ_S^P, and dispersive, γ_S^D, components of the surface tension of the solid.

A DSA100 tensiometer machine with a TC21 temperature control chamber from KRÜSS company was used (see Figure 3). The droplet was photographed by a high-resolution camera (Figure 2). Then, the contact angle was measured by post-processing the image with ADVANCE® built-in software. From the contact angle and properties of the reference liquids, surface tension was calculated using Equation (5).

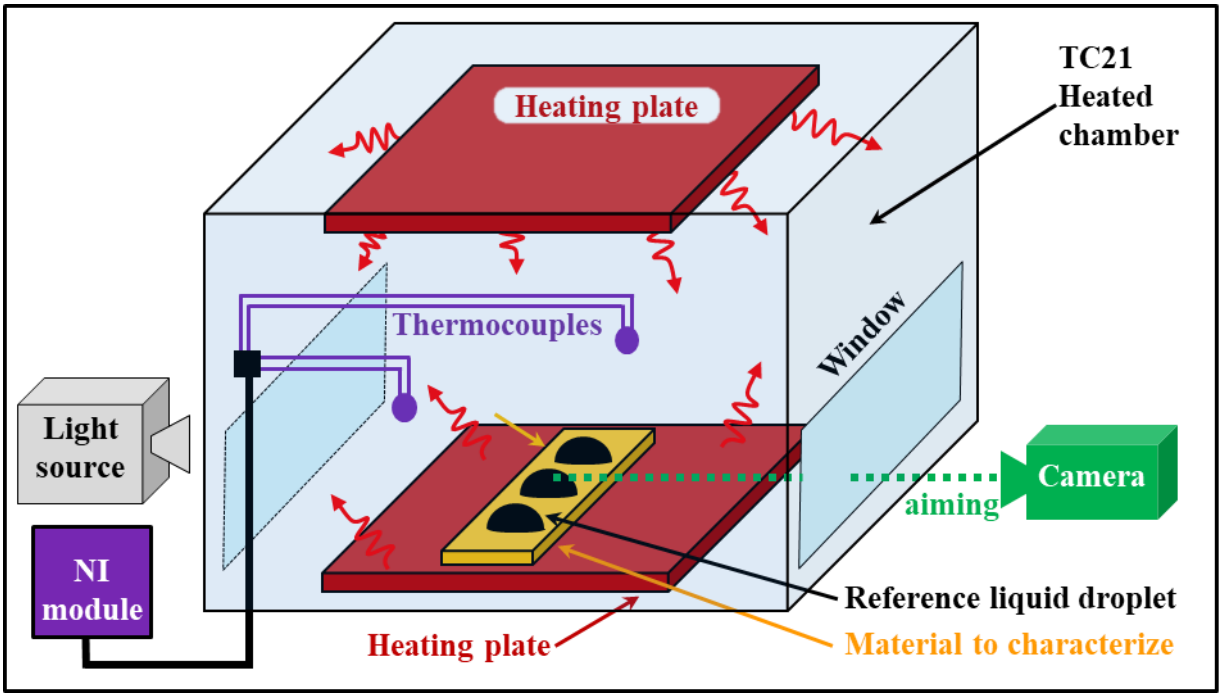

Figure 3 – Sessile drop tensiometer set-up. Additional thermocouples were positioned inside the chamber to assess temperature homogeneity.

Isothermal conditions were imposed with two heating plates, located above and below the chamber. In addition to the tensiometer control thermocouple (reference TP20), to check temperature homogeneity, four 250 µm diameter K-type thermocouples were installed in the chamber (see Figure 3). Temperatures were acquired at a rate of 1 Hz using a National Instruments NI-9212 module. Thermal control of the heating chamber was considered acceptable with a 1.8 °C standard deviation at 79.4 °C.

Amorphous PEKK 60 × 10 × 1 mm plates were molded using a Thermo Scientific HAAKE MiniJet II injection press. The sample was injected at a temperature of 360 °C into a mold at 160 °C with a pressure of 800 bars for 30 s. This thermal cycle quenched the PEKK and prevented crystallization [38]. This amorphous state is representative of the filament deposited in the FFF process. Samples were dried at 105 °C for at least 10 h. Between each measurement, the samples were cleaned with ethanol and acetone. The reference liquids were deposited onto the PEKK surface for testing using a syringe and needle (Figure 3).

The five reference liquids used, with known $\sqrt{\gamma_L^P}$ / $\sqrt{\gamma_L^D}$ ratios, are given in Table 3.

Reference liquid	**Purity**	**Temperature (°C)**	**Polar component γ_L^P (mN/m)**	**Dispersive component γ_L^D (mN/m)**	**References**
water	-	25	50.5	21.6	

		80	44.6	19.1	Constant polarity from [41] was used to extrapolate the γ_L^P and γ_L^D components from the $\gamma_L(T)$ values [42]
ethylene glycol	99.7%	25	21.1	26.2	
		80	18.9	23.4	
glycerol	99.5%	25	26.3	36.8	
		80	24.9	34.9	
diiodomethane	98.5%	25	2.3	47.8	
		80	1.9	40.6	
1-bromona-phthalene	97%	25	0.4	43.8	Temperature dependent polarity with γ_L^P and γ_L^D at 80 °C from [43] and extrapolated to 25 °C
		80	0.8	41.4	

Table 3 – Properties of the reference liquids used in the sessile drop characterization testing.

The reference liquids evaporated at 80 °C. The drop height decreased while the diameter remained constant. This led to a decrease in contact angle with time, as plotted in Figure 4(a). Diiodomethane appears to be the most unreliable (30% deviation in 1 min) while glycerol was the least volatile.

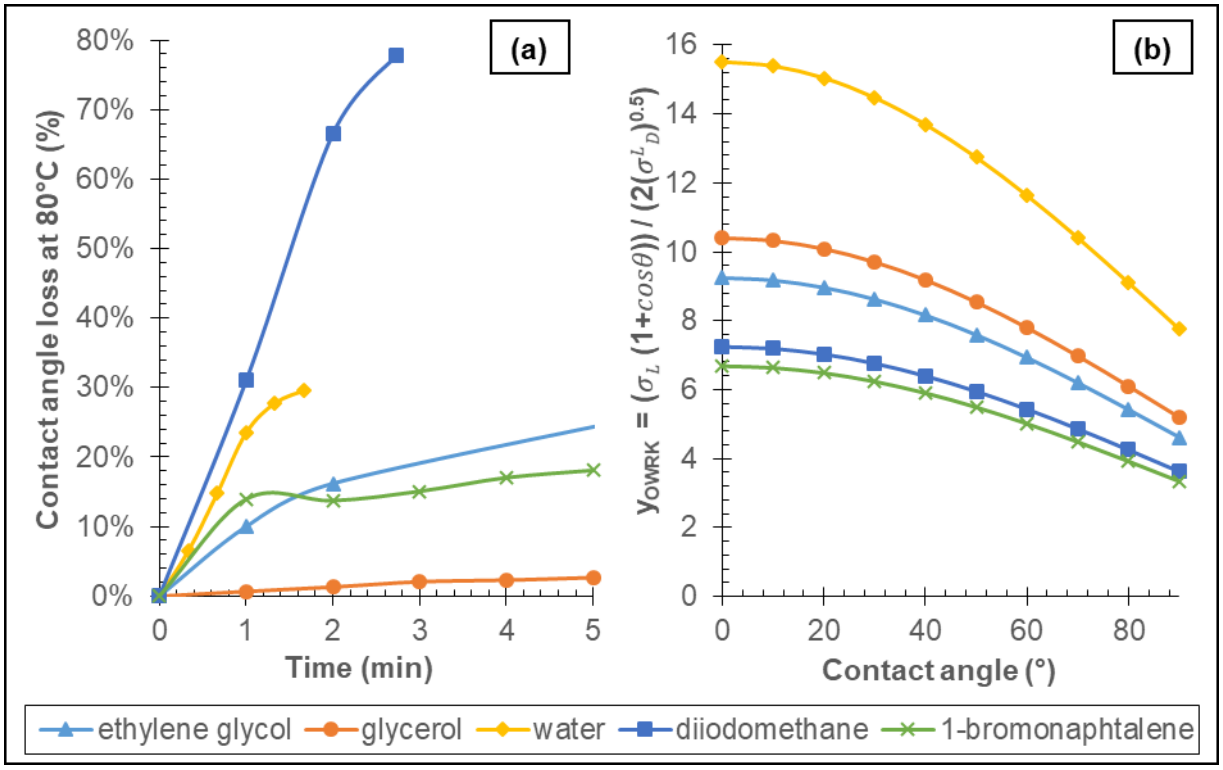

Figure 4 – Study of the sessile drop method range of validity .(a) Contact angle reduction at 80 °C due to liquid evaporation and (b) y_{OWRK} versus contact angle (calculated from Equation (7)) showing lower sensitivity for low contact angles ($\theta < 30°$) and higher sensitivity for high contact angles.

Overall, the measurements should be carried out in less than 1 min. Thermal equilibrium was also tested with thermocouples embedded inside the droplets and showed that a few seconds were necessary to reach a thermal steady state.

Moreover, diiodomethane and 1-bromonaphthalene have a very high wettability on PEKK. Thus, their contact angles were very small ($\theta < 26°$) and their measurements were inaccurate (leading to a maximum standard deviation of 4.6°). Nonetheless, for such small angles, the sensitivity of y_{OWRK} to θ, on the left-hand side term of Equation (5), was very small, as shown in Figure 4(b). Therefore, the errors of the surface tension calculation was minimal ($< 0.9\%$). Because of this low sensitivity, even if diiodomethane had the highest evaporation rate, as indicated in Figure 4(a), it will be considered as a reference liquid in the study at 80 °C for its information contribution to determine better the surface tension. For example, even if the diiodomethane contact angle varied from 17.6 to 12.2° after 1 min, it would cause a difference of 0.7% on the surface tension.

Measurements were performed at 25 and 80 °C. The temperature measurement was averaged for the experiment duration with the five thermocouples. Three PEKK plates were tested at each temperature. Repeatability consisted of at least 10 drops per reference liquid tested, except for diiodomethane and 1-bromonaphthalene, where only a few drops were tested due to the high wettability. There were, in total, around 500 droplets used for the contact angle measurements for the characterization of six samples. y_{OWRK} values are plotted versus x_{OWRK} in Figure 5.

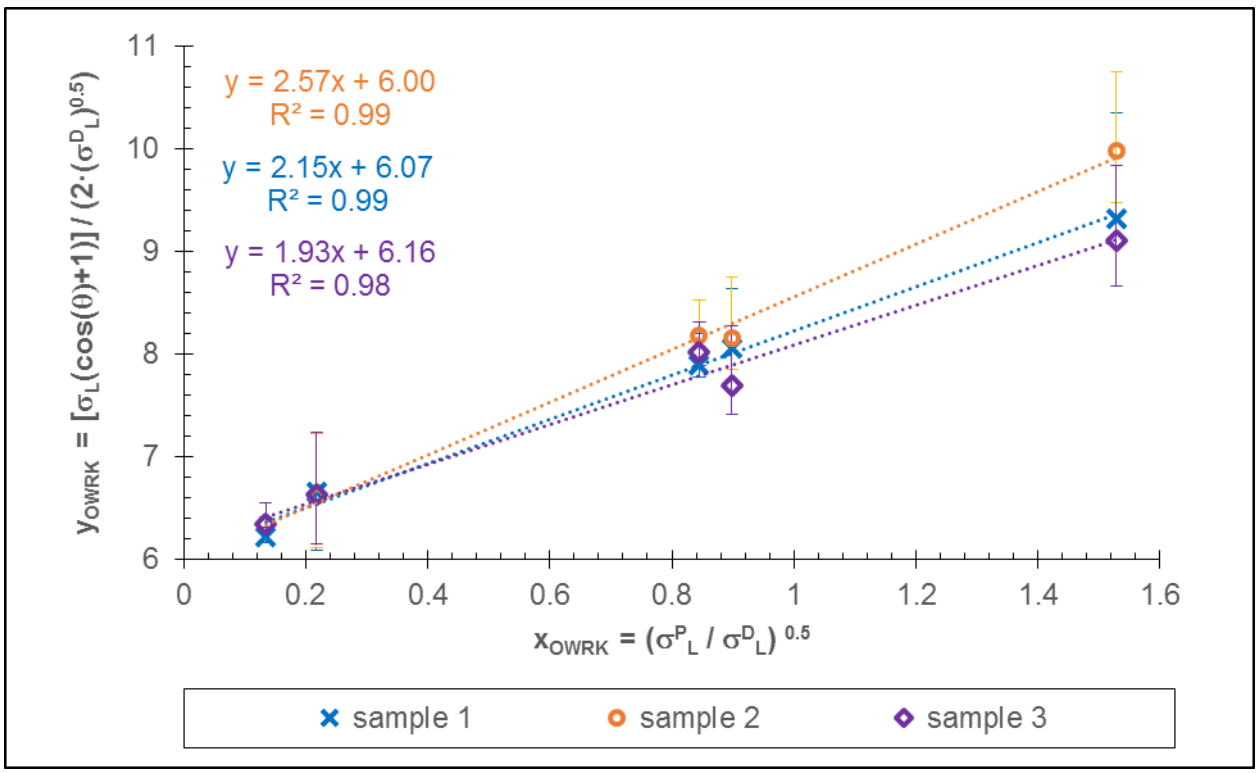

Figure 5 – Sessile drop method at 80 °C based on the OWRK method with five reference liquids. The y_{OWRK} term is plotted versus x_{OWRK} and should fit a straight line as given in Equation (5). The trend line then gives the dispersive and polar components of the surface tension. The alignment of the experimental points confirm the robustness of the method.

The correlation coefficients at 25 °C were in the range of 0.86–0.90. The repeatability appeared to be precise, but not accurate, for the 25 °C experiments. This could be caused by inaccurate polar and dispersive components of the reference liquid obtained from the literature (Table 3). The correlation coefficients at 80 °C were higher, at 0.96–0.99.

The surface tensions obtained with the sessile drop method are presented in Table 4.

Measured temperature	$\boldsymbol{\gamma_S^P}$ **(mN/m)**	$\boldsymbol{\gamma_S^D}$ **(mN/m)**	$\boldsymbol{\gamma_S}$ **(mN/m)**	**Number of samples**
$\mathbf{25.2 \pm 0.3\ °C}$	5.1 ± 0.4	38.5 ± 0.5	43.6 ± 0.8	3
$\mathbf{79.4 \pm 1.8\ °C}$	5.0 ± 1.5	36.9 ± 1.0	41.9 ± 0.6	3

Table 4 – Surface tension with polar and dispersive components results using the sessile drop method.

At 25 °C, they were similar to the values found in the literature for PEKK at room temperature (Table 1). The surface tension measured at 80 °C was slightly lower, confirming that it decreased as the temperature increased. It appears that PEKK is much more dispersive than polar (about 12% polarity at both 25 and 80 °C) and will have good wettability with low-polar liquids, as was confirmed with the very low contact angles with the diiodomethane and 1-bromonaphthalene droplets.

A composite sample with short carbon fibers was also tested with the same procedure at 25 °C. The fiber ratio remains confidential, but is less than 30% by weight. It appeared that the fibers did not influence the surface tension (2% difference compared to neat PEKK). During injection, a neat polymer skin is formed at the surface of the substrate whereas fibers are located in the core of the part [44,45].

2.1.2. Pendant drop method for high temperatures

Pendant drop analysis is suitable for the surface tension measurement of liquids. A drop was suspended from the end of a dosing needle and maintained at static equilibrium. The Young-Laplace equation gives the pressure difference, ΔP, between each side of the drop surface as:

$$\Delta P = (P_{int} - P_{ext}) = \gamma \left(\frac{1}{R_1} + \frac{1}{R_2} \right) \quad (6)$$

where R_1 and R_2 are the curvature radii in two tangent reference planes, as illustrated in Figure 6:

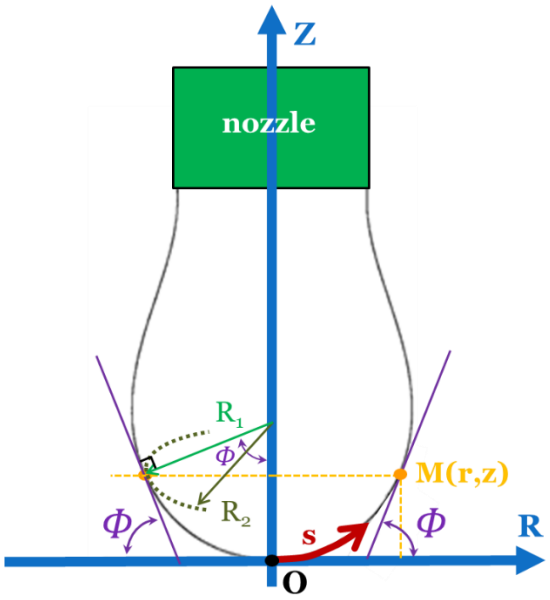

Figure 6 – Pendant drop profile with the two curvature radii and geometrical parameterization.

The profile of the drop is described in Figure 6 in an axisymmetric coordinate system (O, R, Z) [27]. Static equilibrium of the gravitation and surface tension contributions gives:

$$\frac{d\Phi}{ds} = 2k_{apex} - \frac{z \times \Delta\rho \times g}{\gamma} - \frac{sin\Phi}{r} \tag{7}$$

$$\frac{dr}{ds} = cos\Phi \tag{8}$$

$$\frac{dz}{ds} = sin\Phi \tag{9}$$

where s is the curvilinear coordinate, $\Delta\rho$ is the fluid-liquid density difference, g is the gravitational constant, γ is the surface tension, and k_{apex} is a constant linked to the drop profile edge.

Defining the dimensionless variables:

$$r^* = \frac{r}{a};\ z^* = \frac{Z}{a};\ s^* = \frac{s}{a} \tag{10}$$

where $a = \sqrt{\frac{\gamma}{\Delta\rho \times g}}$ is the capillary length.

The Equations (7)–(9) can be reduced to the dimensionless constitutive equation system:

$$\begin{aligned} \frac{d\Phi}{ds^*} &= \frac{2}{B} - z^* - \frac{sin\Phi}{r^*} \\ \frac{dr^*}{ds^*} &= cos\,\Phi \end{aligned} \tag{11}$$

$$\frac{dz^*}{ds^*} = sin\,\Phi$$

where $= \frac{1}{a \cdot k_{apex}}$.

Boundary conditions at the apex, O, of the drop are given as:

$$r^* = z^* = s^* = \Phi = 0 \qquad \text{and} \qquad \frac{sin\Phi}{r^*} = \frac{1}{B} \tag{12}$$

The numerical resolution provides the theoretical profile. The measured experimental profile was corrected to account for the optical and electrical systems and the possible inclination of the drop. The difference between numerical and experimental profiles was then minimized to find a and B [46]. The surface tension was identified from the value of a in Equation (10).

The measurements were carried out using the same DSA100 tensiometer from KRÜSS. The polymer virgin powder was placed inside a temperature-regulated cylinder with a nozzle on one end. The heating chamber was thermally controlled with both the lower and upper hot plates. As seen in Figure 7, the material being characterized is extruded through the nozzle using a piston that is pushed manually; equilibrium was reached manually to form a pendant drop. The droplet shape was recorded with a camera and a light source. A measurement is visible in Figure 8(a) for a pendant drop of PEKK polymer.

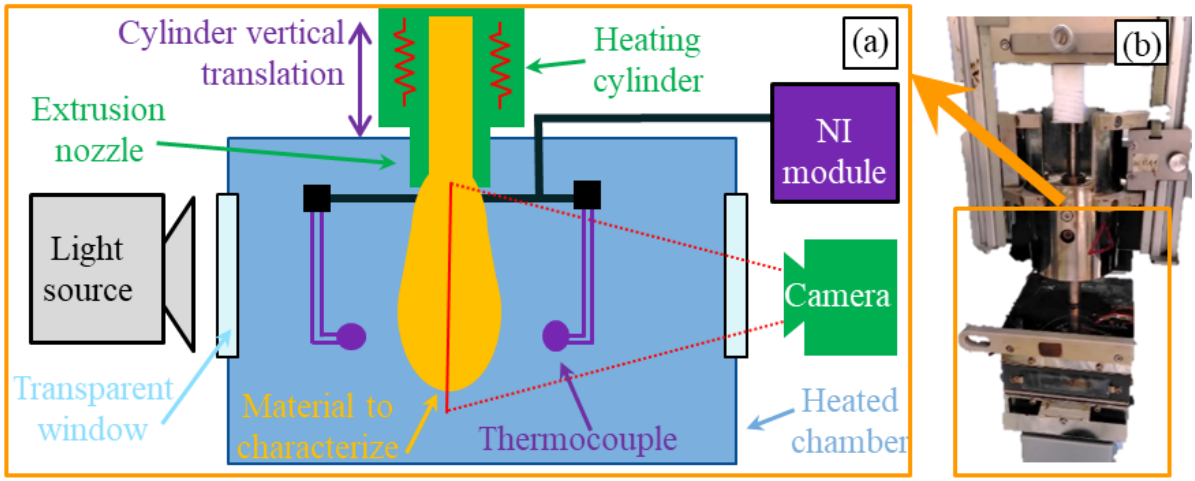

Figure 7 – Pendant drop characterization set-up. (a) Schematic and (b) injection device for the pendant drop method on the tensiometer.

Then ADVANCE® software, distributed with the tensiometer, was used to post-process the videos. The time used for identification was selected when the geometric parameter, B, reached the correct value. KRÜSS software is based on the Song and Springer theory [46]. They propose a wide range of factors, B, that indicate the general morphology of the drop, as illustrated in

Figure 8(b). They specify that the best results are generally obtained with drop profiles that have values of B between 0.6 and 0.7. In our case, the surface tension measurements were determined with the coefficients of B between 0.65 and 0.74.

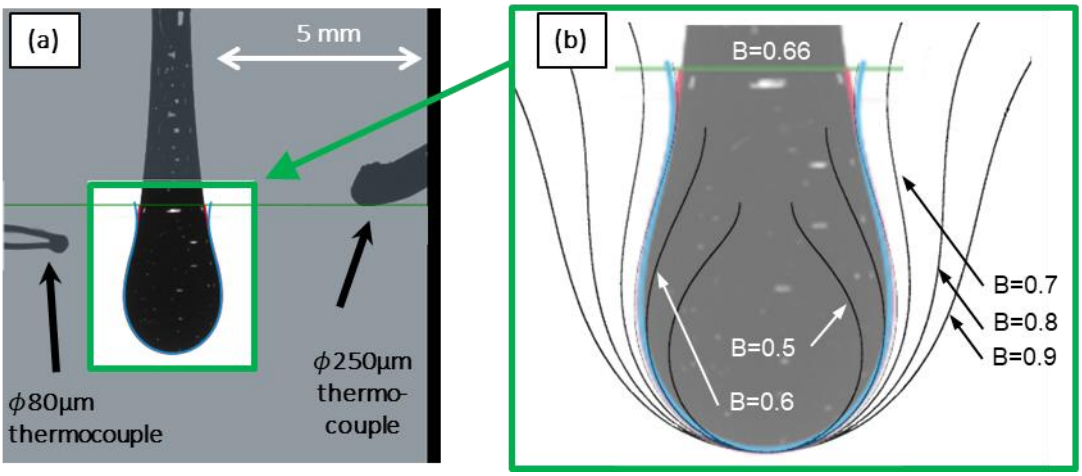

Figure 8 – Pendant drop analysis. Fitting of the theoretical profile (in blue) with the experimental one (in red). (a) For a PEKK pendant drop at $T_{chamber} = 365\ °C$, (b) with a magnified view of non-dimensional pendant drop profiles for different B values inspired from [46].

The measurements were performed at temperatures between 320 °C and 380 °C. Higher temperatures resulted in a chemical evolution in PEKK within a few minutes. Choupin [38] reports in his work that an oxidation layer with a thickness up to 10 nm forms on PEKK, that can therefore be neglected. He suggests that either crosslinking or cuts of the polymer chain are the causes for chemical evolution. This is observed in Figure 9 with the color change from dark yellow to orange, followed by a change to dark brown for highly aged polymers. This polymer evolution was confirmed with differential scanning calorimetry (DSC) analysis, which showed the modification of the enthalpies of crystallization. The glass transition zone and crystallization and fusion peak shapes were also widened. To limit this phenomenon, the temperature of the heating cylinder was set to a value lower than the heated chamber setpoint.

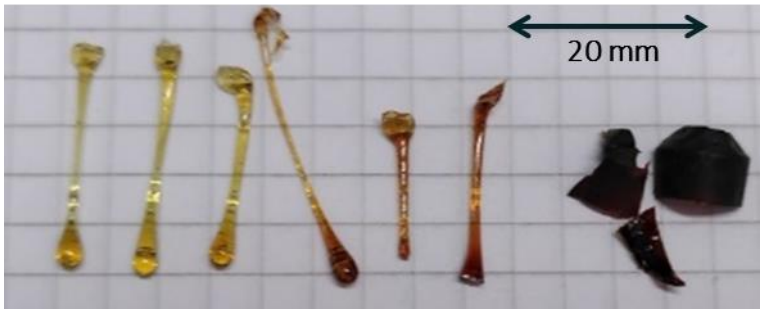

Figure 9 – Chemical evolution of the PEKK pendant drop at high temperatures. (left) Non-aged polymer, (middle) aged polymer and (right) highly aged remains from the heating cylinder.

Additional tests were performed to investigate the thermal management in the chamber. The temperature was recorded while the polymer flowed over the K-type thermocouple positioned in the chamber. The cylinder temperature was set at $T_{cylinder} = 380\ °C$ and the chamber temperature was set at $T_{chamber} = 400\ °C$. In Figure 10, the measured temperature is plotted against time. Initially the thermocouple recorded a steady chamber temperature. At time $t = 6s$, the cylinder was placed in contact with the thermocouple, inducing a sharp decrease from 381 to 363 °C. Thus, the lowest temperature of 363 °C corresponds to the cylinder temperature. Between $t = 10$ and $38\ s$, the temperature was increasing in the chamber, heating the thermocouple. The fluctuations observed in the figure are due to short periods of time where the thermocouple was in contact with the colder cylinder. At stage (a), the PEKK droplet contacted the thermocouple. The temperature of 373 °C, recorded at stage (b), corresponds to the polymer temperature. At stage (c), the polymer droplet detached from the thermocouple. Finally, the temperature increased back to the chamber temperature of 381 °C.

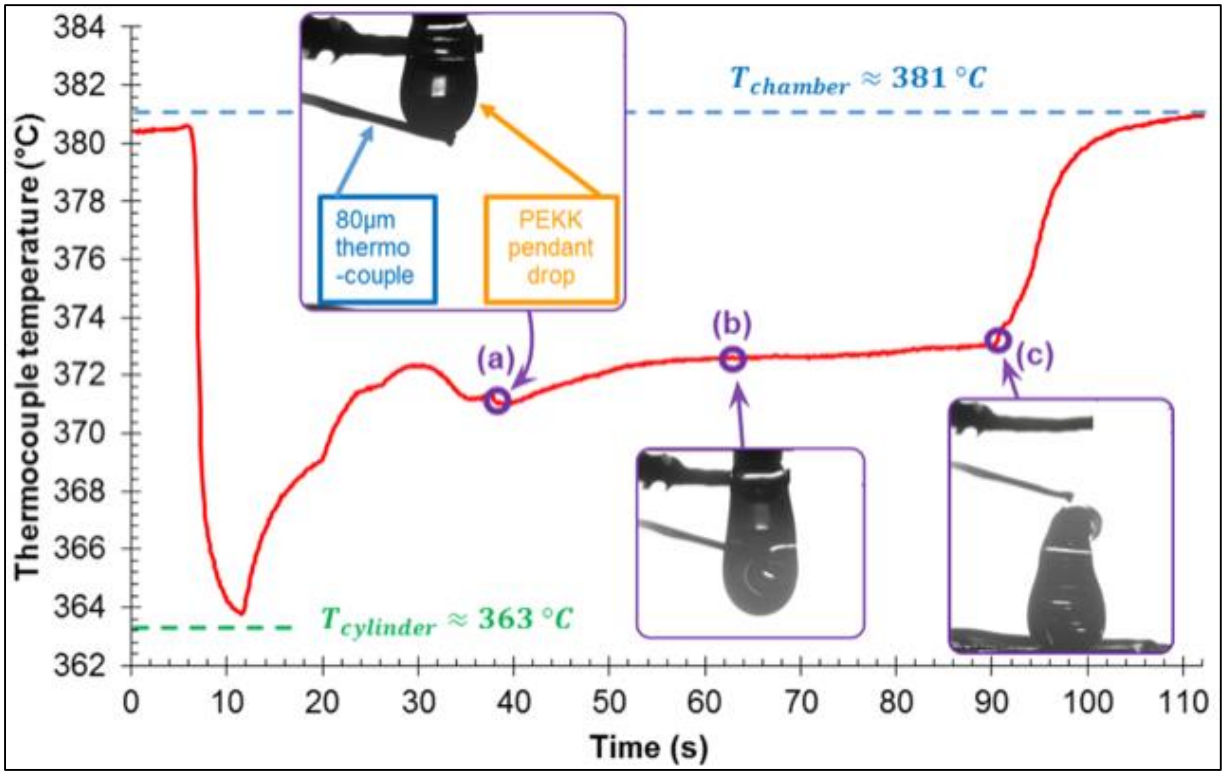

Figure 10 – Temperature recorded by an 80 µm thermocouple positioned inside the chamber. During the experiment, the thermocouple successively contacts the cylinder and the polymer. This is used to determine the chamber, cylinder, and polymer temperatures.

In Figure 10, it appears that the polymer temperature was the average of the heating chamber temperature and the heating cylinder temperature. For each experiment, the chamber temperature was measured with two thermocouples, one with a diameter of 80 µm and another with a 250 µm diameter, positioned approximately 2 mm from the polymer. As in the above experiment (Figure 10), the cylinder temperature was assumed to always be 17 °C less than its setpoint. For each experiment, the polymer temperature used for the characterization was the average of the chamber and cylinder temperatures. Surface tension values were identified with the tensiometer software and the standard deviation was calculated from the repeated pendant drops at the given imposed temperature.

The surface tension characterization results are summarized in Table 5.

Imposed temperature (°C)		**Measured temperature (°C)**		**Temperature (°C)**	**Measured surface tension (mN/m)**	
Cylinder	**Chamber**	**Cylinder**	**Chamber**	**Polymer**	**Polymer**	**Number of tests**
330	340	313	325.5 ± 0.7	319	27.0 ± 3.5	10
330	370	313	353.5 ± 0.7	333	30.1 ± 1.8	16
360	376	343	359.2 ± 0.2	351	26.9 ± 2.8	16
370	370	353	356.4 ± 2.0	355	26.4 ± 1.2	8
366	382	349	364.5 ± 0.3	357	28.5 ± 2.0	6
380	400	363	383.0 ± 0.7	373	26.4 ± 2.3	10

Table 5 – Surface tension measurements using the pendant drop method. The polymer temperature differs from the cylinder and chamber temperature setpoints given by the tensiometer. The reported values are the averages $\pm$ the standard deviation.

The surface tension was constant over the 319 to 373 °C temperature range yielding an average of $\gamma = 27.6\ mN/m$ with a standard deviation of $1.5\ mN/m$. The high viscosity of the polymer prevents tests under 319 °C. The accuracy of the methodology is ensured by the value of the B parameter, from Equation (11). As mentioned previously, the values are close to the ones recommended for this methodology [46]. Thus, we propose to compare the experimental results with the predictions of the Parachor method.

2.1.3. Prediction with Parachor method

Macleod *et al.* [26] propose a relationship between the surface tension, γ, and the density difference between a liquid, ρ, and a gas, ρ_{gas}, with:

$$\gamma = \left(\frac{P}{M_{molar}} (\rho - \rho_{gas}) \right)^4 \tag{13}$$

where γ is the surface tension (in $mN\ /\ m$), ρ is the density of the material (in g/cm^3), ρ_{gaz} is the density of the surrounding gas (in g/cm^3), M_{molar} is the molar mass of the repetitive unit of the polymer (in g/mol), and P is the total Parachor constant of the polymer (in $(cm^3/mol)\cdot(erg/cm^2)^{1/4}$, equivalent to $10^{-27/4}\ m^{5/2}\cdot J^{1/4}\cdot mol^{-1}$). The thermal dependence of density, ρ, influences the surface tension, γ. When the gas density, ρ_{gas}, for the air is three orders of magnitude lower than ρ, surface tension reduces to:

$$\gamma(\mathrm{T}) = \left(\frac{\rho(T)\ \times\ \mathrm{P}}{M_{molar}}\right)^4 \tag{14}$$

The molar mass of the PEKK repetitive unit is 300 $g\cdot mol^{-1}$. The unit Parachor contributions, P_u, are given in Table 7. They were obtained from reference values [30] by studying the repeating unit of the polymer to determine the contribution of each atom or bond.

	Unit Parachor contribution P_u $(cm^3/mol)\cdot(erg/cm^2)^{1/4}$	**Quantity in PEKK repetitive unit N_i**
Carbon	9	20
Hydrogen	15.5	12
Oxygen	19.8	3
6-member ring	0.8	3
Double bond C=C	19.1(*)	9
Double bond C=O	22.3(*)	2
Total Parachor for PEKK polymer $P = \sum(N_i \times P_u)$	644.3	

Table 6 – Unit Parachor contributions used in the surface tension determination with the Parachor method. The contributions for each atom and bond of the macromolecule should be added. (*) the values consider short and linear molecular chains, because no values were found for the very long chains corresponding to the polymers.

As presented in the introduction, other unit Parachor contributions can be found in the literature [31–33], but the total unit Parachor for a PEKK polymer is between $P_u = 634.7$, according to Sugden [31], and $641.1\ (cm^3/mol)\cdot(erg/cm^2)^{1/4}$, according to Vogel [30,33].

The density of amorphous PEKK below T_g was characterized with a DIL L75 PT horizontal dilatometer from LINSEIS using the density at room temperature and the coefficient of thermal expansion from the experiment. For $T > T_g$, the specific volume was measured as a function of temperature at different pressures using the PVT-xT apparatus [47]. The specific volume and density at atmospheric pressure were extrapolated using the Tait model [48–51]:

$$\begin{cases} \rho(kg/m^3) = -0.211 \cdot \mathrm{T(°C)} + 1272.0 \ \text{ for } \mathrm{T} < \mathrm{T_g} \\ \rho(kg/m^3) = -0.683 \cdot \mathrm{T(°C)} + 1339.3 \ \text{ for } \mathrm{T} > \mathrm{T_g} \end{cases} \quad \text{with } T_g = 160°C \text{ [52]} \qquad (15)$$

2.1.4. Summary

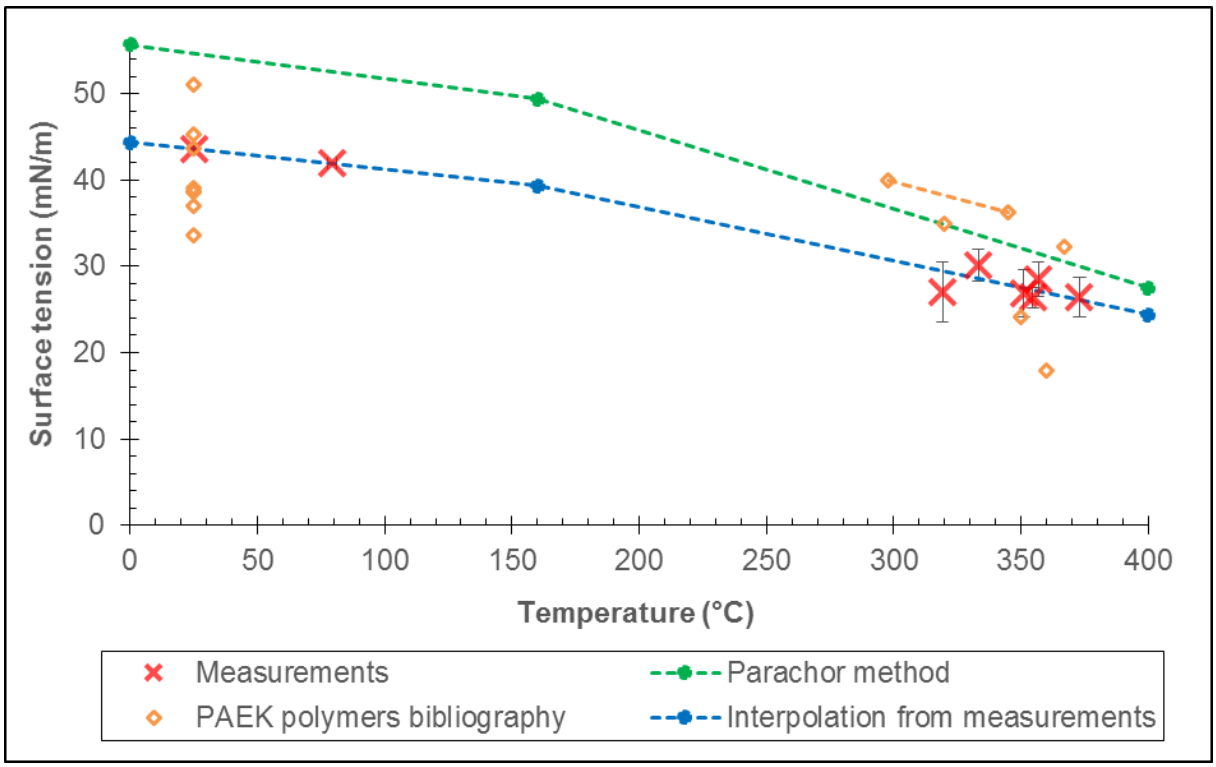

Figure 11 – Surface tension of PEKK over the whole temperature range. The low temperature data were obtained with the sessile drop method, the high temperature data were obtained with the pendant drop method. The values obtained with the Parachor method and a proposed interpolation are also given for any temperature. The obtained data agree with data for other polymers from the PAEK family reported in the literature.

Surface tension is plotted over the whole temperature range in Figure 11. The Parachor model is close to the experimental values for the pendant drop method at high temperatures with 86% accuracy on average. For the sessile drop method at low temperatures, experimental values differ from Parachor ones with a 26% error. Limitations of the Parachor empirical method may be attributed to the molar mass of the total polymer chains, which was not considered. From the experimental point of view, values for PEKK were close to those from the literature for other polymers from the PAEK family. As the temperature increased from 25 to 373 °C, the surface tension value decreased from 43.6 to 26.4 mN/m, representing a 39% variation. This is less obvious in the high temperature range due to the error bars associated with the experimental results. As the surface tension is impacted by the glass transition ($T_g = 160\ °C$), we propose the following interpolation, which is plotted in Figure 11, for the surface tension as a function of temperature.

$$\begin{cases}\gamma(N/m) = -3.0 \cdot 10^{-5} \times \mathrm{T}(°\mathrm{C}) + 4.43 \cdot 10^{-2} & \text{for } \mathrm{T} < \mathrm{T_g} \\ \gamma(N/m) = -6.1 \cdot 10^{-5} \times \mathrm{T}(°\mathrm{C}) + 4.90 \cdot 10^{-2} & \text{for } \mathrm{T} > \mathrm{T_g}\end{cases} \text{ with } T_g = 160\ °C \text{ [52]} \quad (16)$$

With this interpolation, the sensitivity to temperature is higher in the rubbery state than in the glassy region. This corroborates the results found in literature [53].

2.2. Newtonian viscosity measurement

To implement a coalescence model, besides the surface tension, the viscosity is also required. This study will consider only the zero-shear rate viscosity, also named the Newtonian viscosity, because of the Newtonian flow assumption made on the coalescence model. Newtonian viscosity was characterized with a Thermo Scientific HAAKE MARS III rheometer from ThermoFischer, using a plate-plate geometry. The temperature regulation module TM-EL-H allowed the performance of rheological measurements up to 400 °C. In this study, isothermal measurements were carried out at 340, 350, 360, 370, and 380 °C.

Samples were prepared with a Thermo Scientific HAAKE MiniJet II injection press. The samples consisted of disks with a 25 mm diameter and 1.5 mm height. They were molded at 300 bars for 30 s with an injection temperature of 345 °C and a mold regulated at 150 °C. Then, each sample was positioned in the rheometer chamber regulated at the trial temperature. The gap between the two plates was gradually reduced to 1 mm. The sample preparation required around 6 min.

After performing an amplitude sweep to determine the linear domain, a deformation of $\gamma = 5\%$ was chosen. The complex viscosity, $|\mu^*|$, was measured with a frequency sweep from $\omega = 600$ to $0.1\ rad/s$ (Figure 12). For angular frequencies below $\omega = 2\ rad/s$, the viscosity increase, due to the aging of the polymer. Newtonian viscosity, μ_0, was identified at the lowest frequency, and before the aging began.

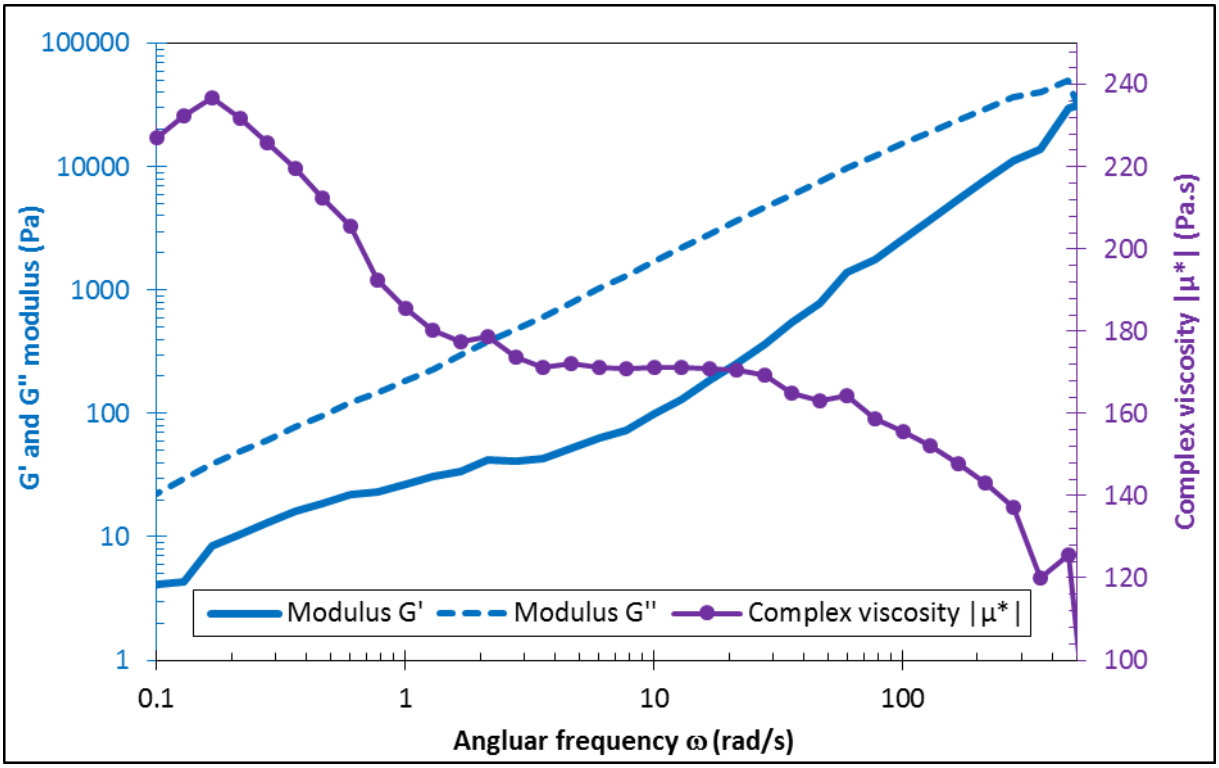

Figure 12 – Frequency sweep experiment with modulus and complex viscosity versus pulsation at 360 °C at a constant deformation amplitude of $\gamma = 5\%$.

Newtonian viscosity is plotted versus temperature in Figure 13. Viscosity values were averaged from five measurements for a given temperature, on the Newtonian plateau visible between $\omega = 4$ and $25\ rad/s$. The standard deviation is obtained from the five measurements, and varies between 0.2% and 2.0% for the five temperatures.

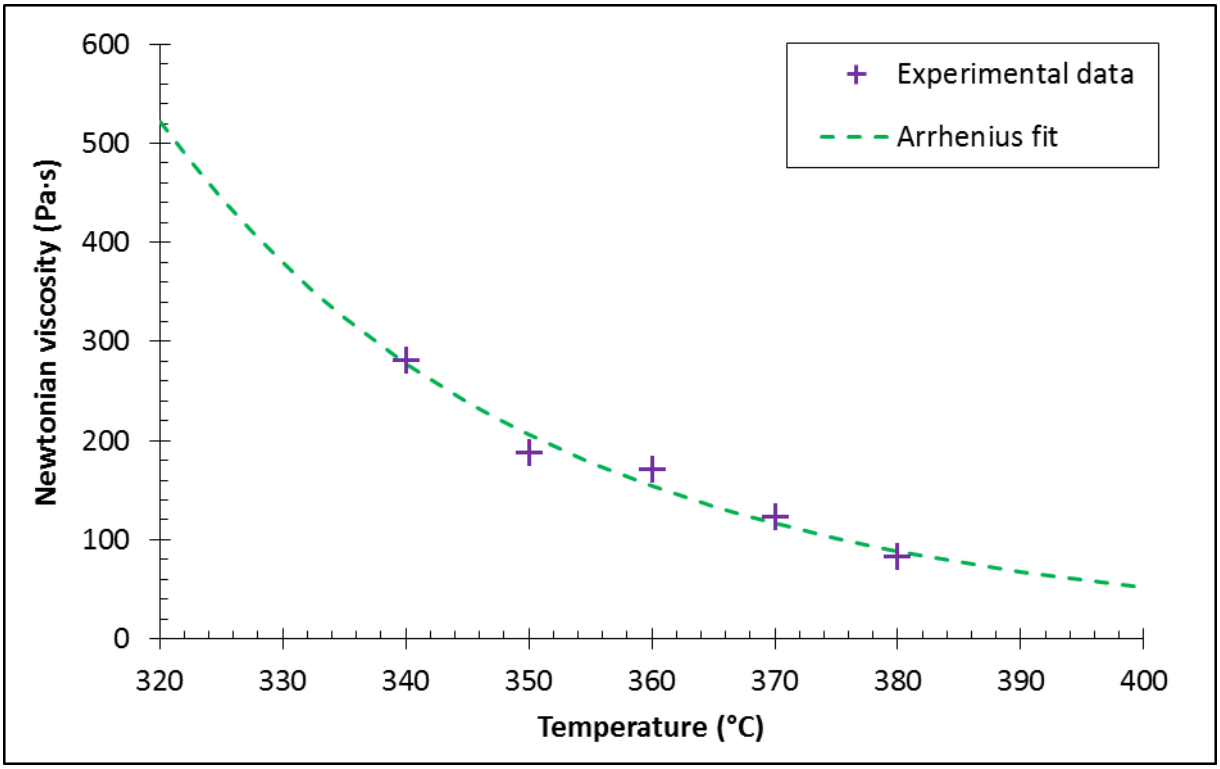

Figure 13 – Newtonian viscosity of PEKK versus temperature around its processing temperature. The experimental data are fitted with an Arrhenius law.

The Newtonian viscosity in Figure 13 has a good fit with the Arrhenius law:

$$\mu_0 = K \times \exp\left(\frac{E_a}{R \times T}\right) \tag{17}$$

with a pre-exponential constant of $K = 2.07 \cdot 10^{-6}\, Pa \cdot s$ and an activation energy of $E_a = 95415\, J\,/\,mol$.

3. Application to the filament coalescence in the FFF process

In the FFF process, polymer adhesion is required between successive paths, consisting of coalescence and interface healing stages. Thus, coalescence is the first prerequisite for proper mechanical bonding. Bakrani Balani *et al.* [54] presented the heterogeneity in the shear rate of the polymer inside the liquefier, and non-Newtonian effects. Nonetheless, the coalescence models classically used in the literature assume a Newtonian viscous behavior and a flow driven by surface tension. In this section, using an existing model from the literature, the characterization results presented above are implemented to quantitatively simulate the coalescence of two PEKK cylinders.

3.1. Coalescence model

Many authors use two spheres as an initial geometry to study coalescence in the FFF process [5,55–60]. This may be adapted to the sintering of powder grains; however, because the FFF process consists of extruding polymers, it would be more appropriate to use a cylinder for the initial geometry.

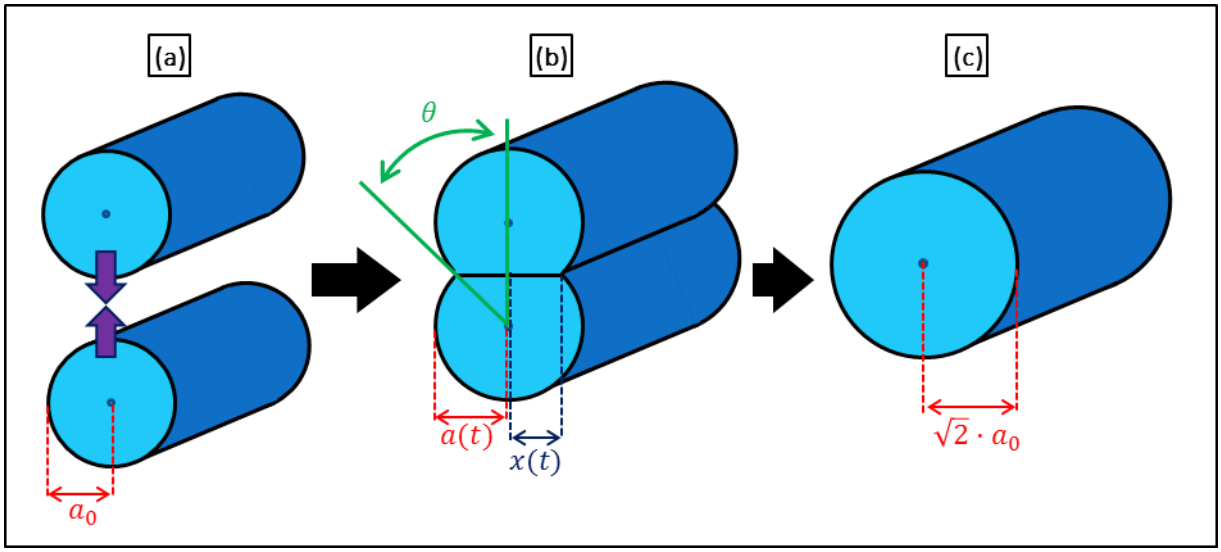

Figure 14 – Coalescence of two infinite cylinders (a) at the initial stage, (b) during coalescence, and (c) when 100% degree of coalescence is accomplished.

Frenkel-Eshelby methodology applied to cylinder geometry was first used by Hirao *et al.* [61]. This study was limited to the initial stage, i.e., a small contact length, and led to an analytical solution of the first order. Without this approximation, the methodology for a cylinder was fully described under a plane strain assumption and solved numerically by Defauchy [23]. The coalescence angle, θ, as defined in Figure 14, follows the nonlinear ordinary differential equation:

$$\frac{d\theta}{dt} = {\tau_c}^{-1} \times F(\theta) \tag{18}$$

where $\tau_c = \mu_0 \times a_0 \,/\, \gamma$ is the capillary time, γ is the surface tension, μ_0 is the Newtonian dynamic viscosity, a_0 is the initial cylinder radius and

$$F(\theta) = \frac{1}{2\sqrt{\pi}} \frac{\left(cos\theta + \frac{sin\theta}{\pi - \theta}\right) \times cos\theta \times \left(\pi - \theta + \frac{\sin(2\theta)}{2}\right)^{0.5}}{\sin^2(\theta) \times (\pi - \theta)} \tag{19}$$

is the Defauchy analytical function.

In this model, the only material parameter is the capillary time, τ_c. The Defauchy analytical function, $F(\theta)$, can be integrated with standard numerical methods. Note that integration should start from a non-zero value for θ to avoid singularity. The COMSOL® Multiphysics implicit backward Euler solver was selected and an initial value of $\theta_{initial} = 10^{-6}\, rad$ was checked to be sufficiently low to ensure convergence.

The cylinder radius is also evolving to ensure volume conservation as:

$$a(\theta) = \left(\frac{\pi \times {a_0}^2}{\pi - \theta + \frac{\sin(2\theta)}{2}} \right)^{1/2} \tag{20}$$

The coalescence length of $x = a \times sin(\theta)$ is used to define a degree of coalescence, $D_c = a \times \sin(\theta) \,/\, \left(\sqrt{2} a_0\right)$. It is plotted versus non-dimensional time, $t^* = t \,/\, \tau_C$, in Figure 15.

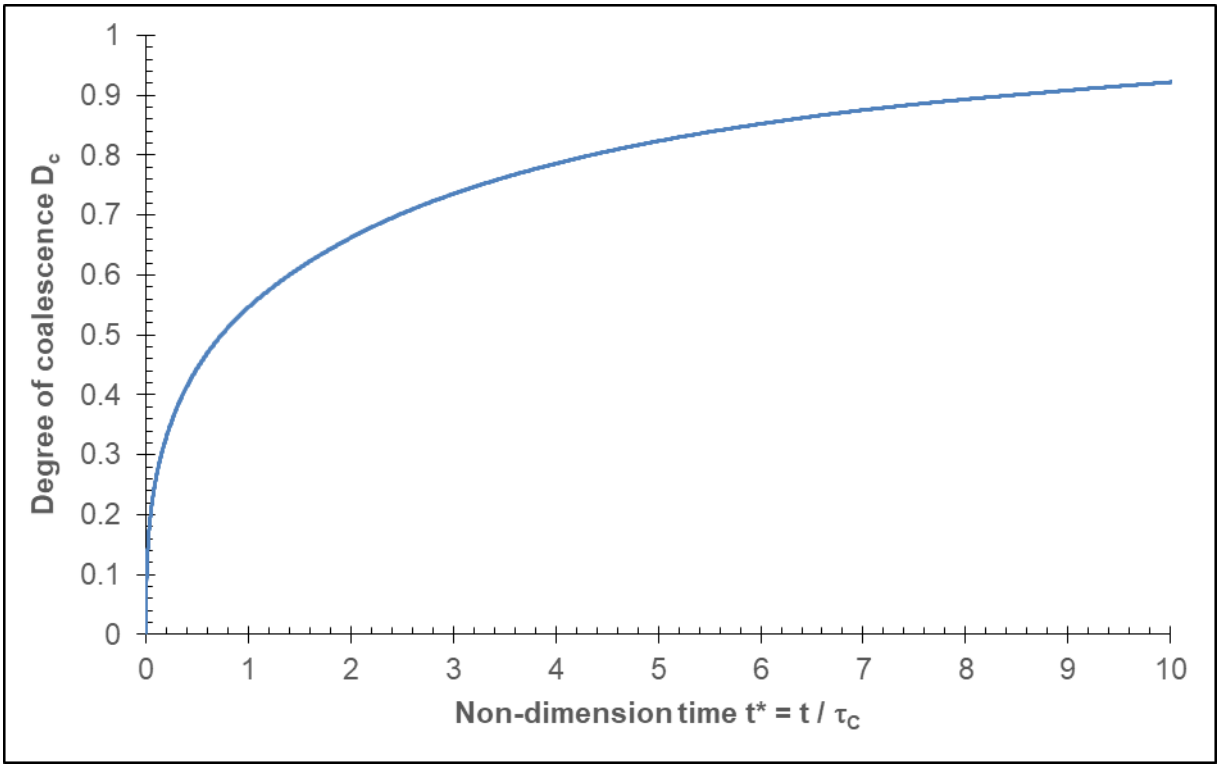

Figure 15 – Degree of coalescence evolution versus non-dimension time, $t^*=t/\tau_c$. From this master curve, results may be obtained for any value of τ_c; the reader should simply multiply the non-dimension time, t^*, by τ_c.

The capillary time is a characteristic time used to calculate the degree of coalescence in dimensional descriptions. A capillary time of $\tau_c = 1$ implies a balanced ratio between the viscosity forces and the surface tension forces on the coalescence kinetics. A dimensional time of $t = \tau_c$ is equivalent to a non-dimensional time of $t^* = 1$ and is therefore equal to a degree of coalescence of $D_c = 0.55$, as shown in Figure 15.

In the following discussion, an initial filament with a radius of $a_0 = 1\ mm$ was considered. Using the surface tension and viscosity characterized in the previous section, the capillary time, τ_c, can be calculated for any temperature. Iso-values of the degree of coalescence and the capillary time are plotted in a time-temperature map in Figure 16. The length of time required to reach coalescence shows the preponderance of the viscous effects, compared to the surface tension, under isothermal conditions. However, over the processing temperatures, the surface tension should not be neglected, for example, at $T = 370\ °C$, the viscosity effect $(\mu_0 \times a_0)$ is only five times as important as the surface tension effect (γ), giving $\tau_C = 5$.

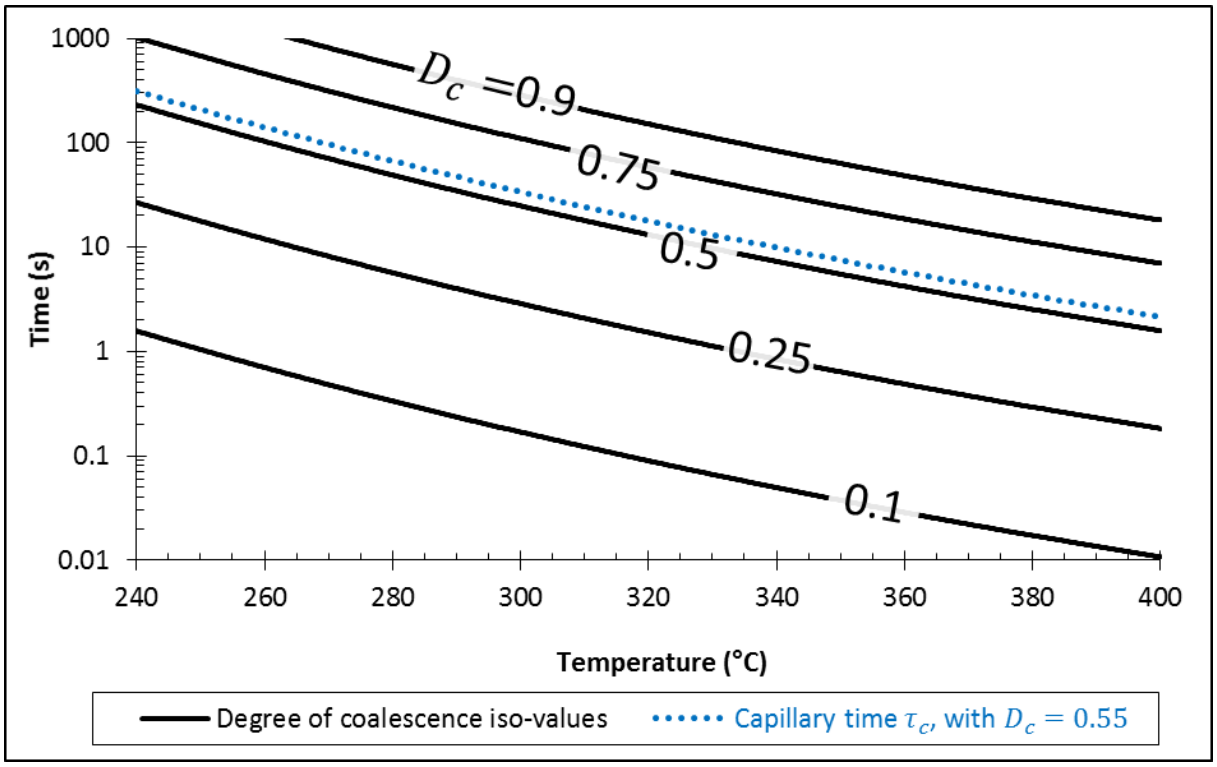

Figure 16 – Time-temperature coalescence diagram with iso-values of the degree of coalescence in a time-temperature map, for $a_0 = 1\ mm$. The results are applicable for isothermal histories.

Figure 16 provides an industrial tool and shows that a high degree of coalescence is very difficult to reach. For example, the filaments must remain at 300 °C for 14 s to reach half-coalescence ($D_c = 0.5$) while only 1.6 s is required at this same temperature to obtain one-quarter coalescence ($D_c = 0.25$). To obtain better mechanical properties for the fabricated part, the aim is to get the highest possible degree of coalescence. Nonetheless, for the FFF process, the objective is not to reach a full coalescence as it would not respect the dimensional geometry needed.

A compromise between the reduction of the porosities and the limitation of the deformation of the filament must then be identified. To increase the coalescence kinetics, different

possibilities could be considered. On the one hand, it is possible to choose process parameters that reduce capillary time, for example with an increase in the processing temperature (see Figure 16). On the other hand, it would also be possible to adapt the formulation of the materials, for example with the addition of fillers which would increase the surface tension, or by reducing the length of the polymer chains which would decrease the viscosity. However, these formulation proposition should be studied because they can also decrease the kinetics of coalescence. Indeed, the addition of fillers can increase the viscosity and the reduction of the polymer chain length also decreases the surface tension [34].

3.2. Extension to FFF non-isothermal process

To be more representative of the actual process, we tested the coalescence model with a time-dependent temperature evolution. The evolution of temperature is extracted from a finite element simulation model describing the cooling down of a stack of filaments with a cross section more representative of the process: a rectangle with fillets. This thermal history was then used to calculate the coalescence kinetics of the coalescence model.

In this section, coalescence will be simulated using the characterized properties for a specific temperature evolution representative of the FFF cycle.

3.2.1. Modeling

A heat transfer finite element model describes the temperature evolution during the FFF process. This model was described in a previous work [62]. The geometry is a wall made of one single filament in the thickness. Even though the initial filament geometry is not a circle, its volume would correspond to a cylinder with a radius of $a_0 = 0.73\ mm$. The 2D simulation domain consists of a cross section of the filament stack and the heating plate substrate. The filaments are successively deposited at an initial temperature of $T_{extrusion} = 360\ °C$. The last deposited filament cools by: (i) conduction with its neighbors and the heating plate at a temperature of $T_{plate} = 160\ °C$, and (ii) air convection in the surrounding chamber which is regulated at $T_{chamber} = 140\ °C$ with a convection coefficient of h_{conv}. Thermal contact resistances of 10^{-4} and $5 \cdot 10^{-5}\ m^2 \cdot K \cdot W^{-1}$ are respectively assumed between filaments and with the heating plate.

This heat transfer model was improved as follows:

- Thermal-dependent density and specific heat was implemented. Density is given versus temperature in Equation (15). Specific heat, C_p, at an amorphous state was characterized with a DSC test by heating at a rate of $5\ K\ /\ min$, from 340 to 380 °C, as follows:

$$C_p(J/(kg \cdot K)) = 3.04 \times \mathrm{T}(°\mathrm{C}) + 1449 \quad \text{for } \mathrm{T} > \mathrm{T_g} \qquad \text{with } T_g = 160\ °C \text{ [52]} \qquad (21)$$

- The thermal conductivity was $\lambda = 0.25\ W\ /\ (m \cdot K)$, as determined with a hot guarded plate between 60 and 140 °C.
- The convection coefficient, h_{conv}, was calculated with an empirical correlation from [63] that is dependent on the chamber temperature, $T_{chamber}$.
- The geometry considered is a wall that is one filament thick and 15 filaments tall (see Figure 17).

The temperature was extracted at the interface of two deposited filaments, as presented in Figure 17. In this figure, temperature decreases quickly between 0 and 10 s, corresponding to the thermal shock between the extruded hot filament and a cold stack. At 10 s, a new filament is deposited above, triggering a temperature increase from 262 to 268 °C.

The temperature was used to compute the thermo-dependent coalescence time, $\tau_c = \mu_0 a_0/\gamma$. Then, the anisothermal coalescence differential Equation (20) was integrated numerically to give the degree of coalescence.

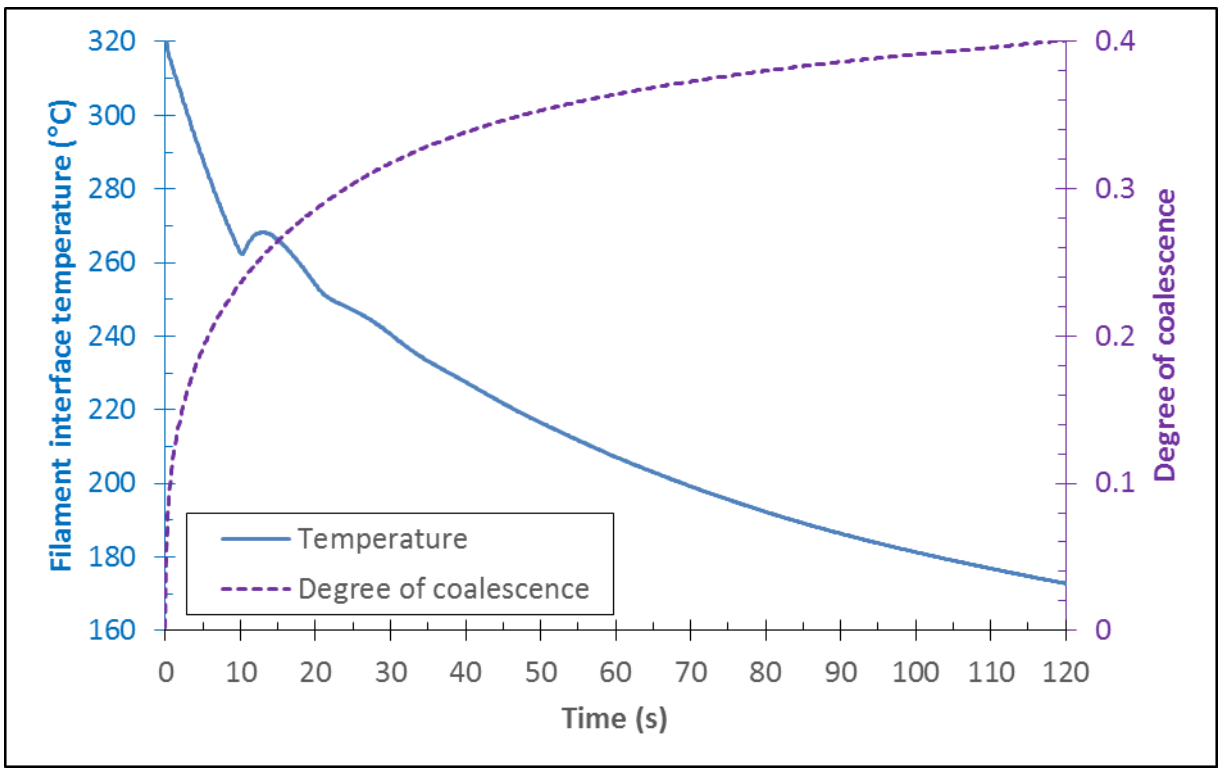

Figure 17 – Temperature history used in the non-isothermal model. The degree of coalescence was integrated, accounting for the temperature dependency of the material properties.

The evolution was much slower when the temperature was below 200 °C, which was justified by the high value of viscosity, and the resulting capillary time.

3.2.2. Importance of the surface tension's sensitivity to temperature

In this section, we will use the coalescence model described earlier to observe the importance of the thermo dependence of the surface tension characterization.

Coalescence evolution was calculated with a thermo-dependent viscosity that considered the thermal history with the process parameters presented in Table 7 and defined in the reference configuration. For surface tension, three different cases were tested, presented in Figure 18:

- The temperature dependency, $\gamma = \gamma(T)$, characterized above and given in Equation (16).
- A constant value of $\gamma = \gamma_{T=25\,°C} = 43.6\,mN/m$ corresponding to the value characterized at room temperature with the sessile drop method (Table 4).
- A constant value of $\gamma = \gamma_{T=373\,°C} = 26.4\,mN/m$, corresponding to the value characterized at high temperature with the pendant drop method (Table 5).

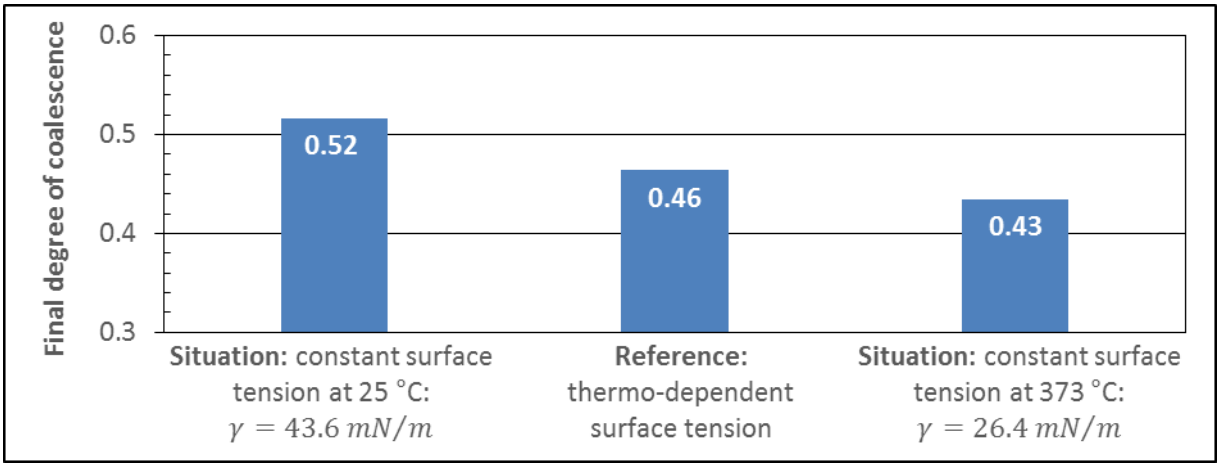

Figure 18 – Final degree of coalescence versus time for different surface tension situations. Neglecting the temperature dependency of the surface tension results in an error varying between 6 and 11% on the final degree of coalescence computation.

The final degree of coalescence that was calculated with the constant surface tension from the sessile drop at 25 °C is overestimated by 11% compared to the reference with a thermo-dependent surface tension. However, the final degree of coalescence that used the constant

surface tension from the pendant drop at 373 °C is underestimated by 6%. These results highlight the importance of the temperature dependency of the surface tension in a coalescence model.

3.2.3. Parametric study

A parametric study was performed on seven different process configurations. The parameters investigated included the time between the deposition of two filaments (linked to nozzle velocity), the extrusion temperature, and the chamber temperature. The reference case was chosen from the experimental optimization of the process with the test bench described in [62]. The final degree of coalescence achieved after 140 s is reported in Table 7:

Configuration	**Reference**	**#1**	**#2**	**#3**	**#4**	**#5**	**#6**
Time between deposition of two filaments (s)	10	60	120	10	10	10	10
Extrusion temperature (°C)	360	360	360	350	370	360	360
Chamber temperature (°C)	140	140	140	140	140	100	60
Final degree of coalescence	0.46	0.26	0.24	0.44	0.49	0.40	0.36

Table 7 – Parametric study with seven different configurations and the calculation of the final degree of coalescence.

As mentioned earlier, porosities need to be minimized to improve mechanical properties, which requires the highest possible degree of coalescence. However, a degree of coalescence equal to 1 is not the objective for the FFF process, because of the geometry that would be too much deformed. It is necessary to find the compromise between the geometrical tolerances of the printed geometry and the decrease of the porosity ratio. Each parameter that influences the degree of coalescence can be studied.

Configurations #1, #2, and the reference show that the time between the deposition of two filaments influences the final coalescence. Indeed, there is 43% reduction from 10 s between two filaments to 60 s and an additional decrease of 8% from 60 to 120 s. The time between the two depositions will increase for larger parts that contain longer layers to print.

In configurations #3, #4, and the reference, the extrusion temperature varies from 350 to 370 °C. This parameter cannot vary over a large range as a cold nozzle would prevent extrusion, while a hot one would degrade the polymer. With this 20 °C variation on the extrusion

temperature, the influence on the final degree of coalescence is low, from $D_{c,final} = 0.44$ at $T_{extrusion} = 350$ °C to $D_{c,final} = 0.49$ at $T_{extrusion} = 370$ °C, representing an increase of 12%.

Configurations #5, #6, and the reference show the importance of a heated chamber in the additive manufacturing process. When the chamber temperature decreased, the printed filament cooled faster and resulted in a lower final coalescence. With $T_{chamber} = 100\ °C$, the degree of coalescence decreased by 13% compared to the reference ($T_{chamber} = 140°C$). With a low-temperature heated chamber (60 °C), representative of many standard 3D-printers, the degree of coalescence decreased by 23% compared to the reference.

4. Conclusion

One of the main drawbacks of the FFF additive manufacturing process is the poor mechanical properties of the parts produced. This is mostly due to an insufficient adhesion between filaments. Adhesion begins with intimate contact, followed by coalescence of the extruded filaments, and finally, interface healing. This work focused on the coalescence phenomenon for filaments fabricated with an aeronautical polymer of the PAEK family. Although different coalescence models exist, they all require Newtonian viscosity and surface tension.

Newtonian viscosity was characterized with standard rheometry. However, the surface tension characterization required special care, as it was performed over a wide range of temperatures (25 to 373 °C). At low temperatures, the surface tension was characterized with the sessile drop method, resulting in $\gamma(25\ °C) = 43.6 \pm 0.8\ mN\ /\ m$, which is consistent with literature, and $\gamma(79\ °C) = 41.9 \pm 0.6\ mN\ /\ m$. At high temperatures, the values obtained by the pendant drop method were between $\gamma = 26.4 \pm 2.3$ and $\gamma = 30.1 \pm 1.8\ mN/m$ for the temperature range from 319 to 373 °C. Finally, the empirical Parachor method was used to interpolate the surface tension over the whole temperature range for a Parachor of $P_u = 644.3\ (cm^3/mol) \cdot (erg/cm^2)^{1/4}$. This over-estimated values at low temperatures but provided more reliable values at high temperatures.

Those characterized properties were implemented in a simplified existing coalescence model for two cylinders. A time-temperature-coalescence diagram was constructed that provided interesting information about the coalescence kinetics under isothermal conditions. This quantified the importance of the viscosity over the surface tension on the coalescence kinetics

when temperature decreased. However, it also showed the necessity to consider surface tension as the temperature approached the processing temperature of the PEKK material.

The coalescence was also implemented in a non-isothermal model used with a previously developed FFF heat transfer model. The results showed that thermal dependency of the surface tension is important. The use of a constant surface tension resulted in an error varying between 6 and 11% on the final degree of coalescence.

Lastly, the final degree of coalescence was calculated from heat transfer simulations based on different processing conditions representative of PEKK additive manufactured parts. This parametric study was carried out on the extrusion temperature, heating chamber temperature, and the time delay between the deposition of two filaments. The results indicated a low sensitivity of extrusion temperature on the final degree of coalescence (12% difference when temperature varied by 20 °C). However, the sensitivity is greater for the time between the deposition of two filaments (48% decrease as time increase from 10 to 120 s) and the heating chamber temperature (23% decrease when temperature decrease from $T_{chamber} = 140$ to $60\ °C$). Since coalescence affects the final mechanical properties due to the porosity, this study illustrated the higher adhesion quality for small parts (when the time between two depositions decreased). Most commercial 3D-printers are limited to heating chamber temperatures of $T_{chamber} = 60\ °C$; however, this study demonstrated the advantage of high temperature heating chambers that reduce the porosity level.

The Defauchy model used in the present work considered a homogenous strain tensor on the cylinder domain. For further improvement, a numerical resolution of the Navier-Stokes equations would be more realistic. Coupled with experimental measurements of the final coalescence level reached within a 3D-printed part, this would confirm the accuracy of the coalescence model.

5. Acknowledgments

This study is part of the FACT project managed by IRT Jules Verne (French Institute in Research and Technology in Advanced Manufacturing Technologies for Composite, Metallic, and Hybrid Structures). The authors wish to associate the industrial and academic partners of this project, respectively AIRBUS, ARKEMA, DAHER, DEDIENNE, EOS, LIEBHERR, SAFRAN, ZODIAC Engineering, CANOE, TOBECA, LTeN, PIMM, CNRS, ENSAM, and the University of Nantes. This project is partly funded by the grant ANR-10-AIRT-02.

The authors also want to thank Violaine Le Louet from CAPACITÉS SAS, a private subsidiary of the University of Nantes, for performing the characterization of the rheological properties and Jean-Philippe Terrier from Gustave Eiffel University for his support and training on the use of the tensiometer.

6. Supplementary materials

Supporting data are available at Mendeley repository, on https://data.mendeley.com/datasets/g9npcnzj3p/2 or http://dx.doi.org/10.17632/g9npcnzj3p.2 .

7. References

[1] T.T. Wohlers, I. Campbell, O. Diegel, R. Huff, J. Kowen, Wohlers Report 2019, 2019.

[2] S.S. Crump, Apparatus and method for creating three-dimensional objects - Patent 5121329, 1992. https://doi.org/10.1016/j.chembiol.2017.08.005.

[3] A. Pandey, S.K. Pradhan, Investigations into Complete Liquefier Dynamics and Optimization of Process Parameters for Fused Deposition Modeling, Mater. Today Proc. 5 (2018) 12940–12955. https://doi.org/10.1016/j.matpr.2018.02.279.

[4] C. Hérard, Les effets de la température lors de la fabrication additive par fdm de composites thermoplastiques renforcés et leurs propriétés mécaniques, Doctoral dissertation, University of Montreal, 2017.

[5] Q. Sun, G.M. Rizvi, C.T. Bellehumeur, P. Gu, Effect of processing conditions on the bonding quality of FDM polymer filaments, Rapid Prototyp. J. 14 (2008) 72–80. https://doi.org/10.1108/13552540810862028.

[6] J. Frenkel, Viscous Flow of Crystalline Bodies under the Action of Surface Tension, J. Phys. 9 (1945) 385. http://ci.nii.ac.jp/naid/10008662610/en/ (accessed June 6, 2018).

[7] J. Eshelby, Discussion of 'Seminar on the Kinetics of Sintering,' Metall. Trans. 185 (1949) 796–813.

[8] O. Pokluda, C.T. Bellehumeur, J. Machopoulos, Modification of Frenkel's Model for Sintering, AIChE J. 43 (1997) 3253–3256. https://doi.org/10.1002/aic.690431213.

[9] R.W. Hopper, Coalescence of Two Equal Cylinders: Exact Results for Creeping Viscous Plane Flow Driven by Capillarity, Commun. Am. Ceram. Soc. 67 (1984) 262–264.

[10] R.W. Hopper, Coalescence of Two Viscous Cylinders by Capillarity: Part I, Theory, Am. Ceram. Soc. 76 (1993) 2947–52.

[11] R.W. Hopper, Coalescence of Two Viscous Cylinders by Capillarity: Part II, Shape Evolution, Am. Ceram. Soc. 76 (1993) 2953–2960.

[12] S. Bakrani Balani, C. Arthur, C. France, N. Valerie, Influence of parameters controlling the extrusion step in Fused Filament Fabrication (FFF) process applied to polymers using numerical simulation, in: AIP Conf. Proc. 1960 - 21st Int. ESAFORM Conf. Mater. Forming, Parlermo, Italy, 2018. https://doi.org/10.1063/1.5008034.

[13] V. Kishore, X. Chen, C. Ajinjeru, A.A. Hassen, J. Lindahl, J. Failla, V. Kunc, C. Duty, Additive Manufacturing of High Performance Semicrystalline Thermoplastics and Their

Composites, Proc. 27th Annu. Int. Solid Free. Fabr. Symp. – An Addit. Manuf. Conf. (2016) 906–915.

[14] S. Bakrani Balani, Additive manufacturing of the high-performance thermoplastic: Experimental study and numerical simulation of the Fused Filament Fabrication, Doctoral dissertation, University of Toulouse, 2019. https://doi.org/10.13140/RG.2.2.18816.89609.

[15] B.B. Sauer, N. V. Dipaolo, Surface Tension and Dynamic Wetting of Polymers Using the Wihelmy Method : Applications to High Molecular Weights and Elevated Temperatures, J. Colloid Interface Sci. 144 (1991).

[16] M.R. Bowditch, S.J. Shaw, Adhesive bonding for high performance materials, Adv. Perform. Mater. 3 (1996) 325–342. https://doi.org/10.1007/BF00136795.

[17] S.W. Ha, R. Hauert, K.H. Ernst, E. Wintermantel, Surface analysis of chemically-etched and plasma-treated polyetheretherketone (PEEK) for biomedical applications, Surf. Coatings Technol. 96 (1997) 293–299. https://doi.org/10.1016/S0257-8972(97)00179-5.

[18] H.M.S. Iqbal, S. Bhowmik, R. Benedictus, Surface modification of high performance polymers by atmospheric pressure plasma and failure mechanism of adhesive bonded joints, Int. J. Adhes. Adhes. 30 (2010) 418–424. https://doi.org/10.1016/j.ijadhadh.2010.02.007.

[19] N. Bhatnagar, S. Jha, S. Bhowmik, Energy dispersive spectroscopy study of surface modified PEEK, Adv. Mater. Lett. 2 (2011) 52–57. https://doi.org/10.5185/amlett.2010.12188.

[20] S. Kluska, E. Pamuła, S. Jonas, Z. Grzesik, Surface modification of polyetheretherketone by helium/nitrogen and nitrous oxide plasma enhanced chemical vapour deposition, High Temp. Mater. Process. 33 (2014) 147–153. https://doi.org/10.1515/htmp-2013-0022.

[21] Y. Su, M. de Rooij, W. Grouve, R. Akkerman, The effect of titanium surface treatment on the interfacial strength of titanium – Thermoplastic composite joints, Int. J. Adhes. Adhes. 72 (2017) 98–108. https://doi.org/10.1016/j.ijadhadh.2016.10.007.

[22] B.B. Sauer, G.T. Dee, Surface Tension and Melt Cohesive Energy Density of Polymer Melts Including High Melting and High Glass Transition Polymers, (2002) 7024–7030. https://doi.org/10.1021/ma0202437.

[23] D. Defauchy, Simulation du procédé de fabrication directe de pièces thermoplastiques par fusion laser de poudre, Doctoral dissertation, Paris Institue of Technology, ENSAM, 2013.

[24] L. Eötvös, Ueber den Zusammenhang der Oberflächenspannung der Flüssigkeiten mit ihrem Molecularvolumen, Ann. Phys. (1886) 448.

[25] E.A. Guggenheim, The Principle of Corresponding States, J. Chem. Phys. 13 (1945) 253–261.

[26] D. Macleod, On a relation between surface tension and density, Trans. Faraday Soc. 19 (1923) 38–41.

[27] D.G. Legrand, G.L. Gaines, The molecular weight dependence of polymer surface tension, J. Colloid Interface Sci. 31 (1969) 162–167. https://doi.org/10.1016/0021-9797(69)90322-1.

[28] S. Wu, Interfacial and Surface Tensions of Polymers, J. Macromol. Sci. Part C. 10 (1974) 1–73. https://doi.org/10.1080/15321797408080004.

[29] N.R. Demarquette, F.T. Da Silva, S.D. Brandi, D. Gouvêa, Surface Tension of Polyethylene Used in Thermal Coating, Polym. Eng. Sci. 40 (2000) 1663–1671.

[30] O.R. Quayle, The Parachors of Organic Compound - An Interpretation and Catalogue, Chem. Rev. 53 (1953) 439–589. https://doi.org/10.1021/cr60166a003.

[31] S. Sugden, A relation between surface tension, density, and chemical composition, J. Chem. Soc. Trans. 125 (1924) 1177–1189. https://doi.org/10.1039/CT9242501177.

[32] S.A. Mumford, J.W.C. Phillips, The Evaluation and Interpretation of Parachors, J. Chem. Soc. (1929) 2112–2133.

[33] A.I. Vogel, Physical Properties and Chemical Constitution., J. Chem. Soc. 83 (1934) 333–341.

[34] G. Cazaux, Faisabilité des procédés LCM pour l'élaboration de composites renfort continu à matrice thermoplastique polyamide, Doctoral dissertation, Le Havre University, 2017.

[35] J.M. Dealy, R.G. Larson, Structure and Rheology of Molten Polymers, Hanser Publishers, Munich, 2006. https://doi.org/10.3139/9783446412811.fm.

[36] M. Doi, Explanation for the 3. 4-Power Law for Viscosity of Polymeric Liquids on the Basis of the Tube Model., J. Polym. Sci. Part A-2, Polym. Phys. 21 (1983) 667–684. https://doi.org/10.1002/pol.1983.180210501.

[37] ARKEMA, KEPSTAN PEKK Brochure - A basic overview of grades and performance properties, brochure, 2018. https://www.extrememateriales-arkema.com/en/product-families/kepstan-pekk-polymer-range/.

[38] T. Choupin, Mechanical performances of PEKK thermoplastic composites linked to their processing parameters, Doctoral Thesis, Paris Institue of Technology, ENSAM, 2017.

[39] M. Coulson, L. Quiroga Cortés, E. Dantras, A. Lonjon, C. Lacabanne, Dynamic rheological behavior of poly(ether ketone ketone) from solid state to melt state, J. Appl. Polym. Sci. 135 (2018) 1–7. https://doi.org/10.1002/app.46456.

[40] D.K. Owens, R.C. Wendt, Estimation of the Surface Free Energy of Polymers, J. Appl. Polym. Sci. 13 (1969) 1741–1747.

[41] KRÜSS, ADVANCE Software - database for Drop Shape Analyzers, (2014).

[42] DataPhysics Instruments - Measurement equipment for surface and interfacial science, (n.d.). https://www.dataphysics-instruments.com/Downloads/Surface-Tensions-Energies.pdf.

[43] C. Rulison, Effect of Temperature on the Surface Energy of Solids - Kruss - application report - Scientific Augustine, 2005. https://doi.org/10.1016/s0026-0576(03)90164-4.

[44] J. Agassant, R. Blanc, S. Philipon, M. Vincent, H. Alglave, R. Muller, D. Froelich, Injection molding of reinforced thermosets: Fiber orientation observations and flow calculation, Int. Polym. Process. 2 (1987) 21–27. http://library1.nida.ac.th/termpaper6/sd/2554/19755.pdf.

[45] T. Papathanasiou, Flow-induced alignment in injection molding of fiber-reinforced polymer composites, in: Flow-Induced Alignment Compos. Mater. - Papathanasiou TD, Guell DC, Ed., Cambridge: Woodhead Publishing Ltd, 1997: pp. 112–165. https://doi.org/10.1201/9781439822739.ch4.

[46] B. Song, J. Springer, Determination of Interfacial Tension from the Profile of a Pendant

Drop Using Computer-Aided Image Processing - 1. Theoretical, 184 (1996) 64–76.

[47] B. Pignon, X. Tardif, N. Lefèvre, V. Sobotka, N. Boyard, D. Delaunay, A new PvT device for high performance thermoplastics: Heat transfer analysis and crystallization kinetics identification, Polym. Test. 45 (2015) 152–160. https://doi.org/10.1016/j.polymertesting.2015.05.013.

[48] P. Tait, Physics and Chemistry of the voyage of H.M.S Challenger, Londres. 2 (1888).

[49] G. Tammann, Über die Abhängigkeit der Volumina von Lösungen vom Druck, Z. Phys. Chemi. 17 (1895) 620.

[50] J.H. Dymond, R. Malhotra, The Tait equation: 100 years on, Int. J. Thermophys. 9 (1988) 941–951. https://doi.org/10.1007/BF01133262.

[51] B. Pignon, Cristallisation des polymères semi-cristallins en condition thermique extrême, Doctoral dissertation, University of Nantes, LTEN, 2015.

[52] Arkema, Datasheet Kepstan 6000 Series, 2013.

[53] S. Wu, Chapter 3 - Interfacial and Surface Tensions of Polymer Melts and Liquids, in: Polym. Interface Adhes., 1982: pp. 67–132.

[54] S. Bakrani Balani, F. Chabert, V. Nassiet, A. Cantarel, Influence of printing parameters on the stability of deposited beads in fused filament fabrication of poly(lactic) acid, Addit. Manuf. 25 (2019) 112–121. https://doi.org/10.1016/j.addma.2018.10.012.

[55] C. Bellehumeur, L. Li, Modeling of Bond Formation Between Polymer Filaments in the Fused Deposition Modeling Process, J. Manuf. Process. 6 (2004) 170–178. https://doi.org/10.1016/S1526-6125(04)70071-7.

[56] D.O. Kazmer, T.J. Coogan, J. Mead, C. Barry, S. Johnston, R. Malloy, M. Sobkowicz-Kline, J. Vangness, P. Casey, D. Rondeau, A. Moshe, A Protocol for Filament Production and Use in Fused Deposition Modeling, Spe Antec. (2016) 881–886.

[57] M. Faes, E. Ferraris, D. Moens, Influence of Inter-layer Cooling time on the Quasi-static Properties of ABS Components Produced via Fused Deposition Modelling, Procedia CIRP. 42 (2016) 748–753. https://doi.org/10.1016/j.procir.2016.02.313.

[58] B. Brenken, E. Barocio, A. Favaloro, V. Kunc, R.B. Pipes, Fused filament fabrication of fiber-reinforced polymers: A review, Addit. Manuf. 21 (2018) 1–16. https://doi.org/10.1016/j.addma.2018.01.002.

[59] L. Li, Q. Sun, C. Bellehumeur, P. Gu, Investigation of bond formation in FDM process, Solid Free. Fabr. Proc. (2002) 400–407. https://doi.org/10.1108/13552540810862028.

[60] S. Bakrani Balani, C. France, N. Valerie, Toward improvement of the properties of parts manufactured by FFF (fused filament fabrication) through understanding the influence of temperature and rheological behaviour on the coalescence phenomenon, in: AIP Conf. Proc. 1896, 2017.

[61] K. Hirao, M. Tomozawa, Kinetics of Crack Tip Blunting of Glasses, J. Am. Ceram. Soc. 70 (1987) 43–48. https://doi.org/10.1111/j.1151-2916.1987.tb04851.x.

[62] A. Lepoivre, N. Boyard, A. Levy, V. Sobotka, Heat Transfer and Adhesion Study for the FFF Additive Manufacturing Process, Procedia Manuf. 47 (2020) 948–955. https://doi.org/10.1016/j.promfg.2020.04.291.

[63] F.P. Incropera, T.L. Bergman, A.S. Lavine, D.P. DeWitt, Fundamentals of Heat and Mass Transfer, John Wiley & Sons, Inc., 2011.

https://doi.org/10.1073/pnas.0703993104.